# Meshless Large Eddy Simulation of Propeller-Wing Interactions with Reformulated Vortex Particle Method

Eduardo J. Alvarez\* and Andrew Ning<sup>†</sup>

Brigham Young University, Provo, Utah, 84602

The vortex particle method (VPM) has gained popularity in recent years due to a growing need to predict complex aerodynamic interactions during preliminary design of electric multirotor aircraft. However, VPM is known to be numerically unstable when vortical structures break down close to the turbulent regime. In recent work, the VPM has been reformulated as a large eddy simulation (LES) in a scheme that is both meshless and numerically stable, without increasing its computational cost. In this study, we build upon this meshless LES scheme to create a solver for interactional aerodynamics. Propeller blades are introduced through an actuator line model following well-established practices for LES. A novel, vorticity-based, actuator surface model (ASM) is developed for wings, which is suitable for propeller-wing interactions when a wake impinges on the surface of a wing. This ASM imposes the no-flow-through condition at the airfoil centerline by calculating the circulation that meets this condition and by immersing the associated vorticity in the LES following a pressure-like distribution. Extensive validation of propeller-wing interactions is presented simulating a tailplane with tip-mounted propellers and a blown wing with propellers mounted mid-span.

	Nomenclature		J	Advance ratio, $U_{\infty}/nD$	
Physical Variables and Properties		n	Revolutions per second 1/	's	
$\alpha$	Angle of attack (AOA)	deg	R	Radius	n
ω	Vorticity field, $\omega(\mathbf{x}, t)$	1/s	r	Radial position r	n
$oldsymbol{\omega}^*$	Non-dimensional vorticity, $\omega^* \equiv \omega D/V_{\text{disk}}$	:	t		s
$\delta_e$	Elevator deflection	deg	-	Magnitude of freestream velocity m/	
$\eta$	Propulsive efficiency, $\eta = TU_{\infty}/2\pi nQ$			ematical Variables and Functions	5
Γ	Circulation	$m^2/s$			10
u	Velocity field, $\mathbf{u}(\mathbf{x}, t)$	m/s	$\Gamma_p$		
X	Position	m	$\mathbf{E}_{\mathrm{adv}}$	SFS vorticity advection, $(\mathbf{E}_{adv})_i \equiv \partial T'_{ij}/\partial x_j$ 1/s	_
Re	Reynolds number		$\mathbf{E}_{\mathrm{str}}$	SFS vortex stretching, $(\mathbf{E}_{\text{str}})_i \equiv -\partial T_{ij}/\partial x_j$ 1/s	i <sup>2</sup>
ν	Kinematic viscosity	$m^2/s$	$\mathbf{x}_p$		n
ho	Density	$kg/m^3$	$\sigma$	Filter width (smoothing radius or core size)	n
b	Wing span	m	$\sigma_p$	Filter width at <i>p</i> -th particle, $\sigma_p(t) \equiv \sigma(\mathbf{x}_p, t)$ r	n
c	Chord length	m	ζ	Radial basis function	
$c_{\ell}$	Sectional lift coefficient, $c_{\ell} = \ell/\frac{1}{2}\rho U_{\infty}^2 c$		$\zeta_{\sigma}$	Filter kernel, $\zeta_{\sigma}(\mathbf{x}) \equiv \zeta(\ \mathbf{x}\ /\sigma)/\sigma^3$ 1/m	3
$C_D$	drag coefficient, $C_D = D/\frac{1}{2}\rho U_{\infty}^2 bc$		$C_d$	SFS model coefficient, $C_d(\mathbf{x}, t)$	
$c_d$	Sectional drag coefficient, $c_d = d/\frac{1}{2}\rho U_{\infty}^2 c$		f, g	VPM formulation parameters	
$C_L$	lift coefficient, $C_L = L/\frac{1}{2}\rho U_{\infty}^2 bc$		a	Regularizing function, $g_{\sigma}(\mathbf{x}) = 4\pi \int_{0}^{\ \mathbf{x}\ /\sigma} \zeta(t) t^2 dt$	
$c_n$	Normal force coefficient, $c_n = n/\frac{1}{2}\rho U_{\infty}^2 c$		$g_{\sigma}$		
$C_Q$	Torque coefficient, $C_Q = Q/\rho n^2 d^5$		$n_{\rm blade}$	Number of blade elements per blade	
$C_T$	Thrust coefficient, $C_T = T/\rho n^2 d^4$		$N_{ m sheds}$	Number of particle sheds per revolution	
$c_t$	Tangential force coefficient, $c_t = t/\frac{1}{2}\rho U_{\infty}^2 c$	;	$N_{\rm steps}$	Number of time steps per revolution	
D	Diameter	m	$T_{ij}$	SFS vorticity stress tensor, $T_{ij} = \overline{u_i \omega_j} - \overline{u_i} \overline{\omega_j}$ m/s	,2

<sup>\*</sup>Ph.D., Currently: Aeronautical R&D Engineer, Whisper Aero Inc., AIAA Member. Corresponding author, edoalvarezr@gmail.com.

<sup>&</sup>lt;sup>†</sup>Associate Professor, Department of Mechanical Engineering, AIAA Associate Fellow.

# I. Introduction

The vortex particle method (VPM) [1] is a meshless approach to computational fluid dynamics (CFD) solving the Navier-Stokes equations in their velocity-vorticity form. The VPM uses a Lagrangian scheme, which not only avoids the hurdles of mesh generation, but it also conserves vortical structures over long distances with minimal numerical dissipation while often being one to two orders of magnitude faster than conventional mesh-based CFD [2]. In recent years, VPM has gained popularity due to a growing need to predict complex aerodynamic interactions during preliminary design of electric multirotor aircraft. For instance, VPM has recently been used as a mid-fidelity tool for rotor-rotor interactions [3–7], electric vertical takeoff and landing (eVTOL) [8], stacked propeller [9], tiltrotors [10], and multirotor tiltwing [11]. However, VPM is known to be numerically unstable when vortical structures break down close to the turbulent regime.

In recent work by the authors [2, 12], the VPM has been reformulated as a large eddy simulation (LES) in a scheme that is numerically stable, without increasing its computational cost. The new method, referred to as the *reformulated VPM* or rVPM, uses a new set of governing equations derived directly from the LES-filtered Navier-Stokes equations. The new equations reinforce conservation of mass and angular momentum by reshaping the vortex elements subject to vortex stretching. The rVPM, coupled with a novel subfilter-scale model of vortex stretching, provides an LES scheme that is meshless and numerically stable. As shown in References [2] and [12], the rVPM is a meshless LES that (1) efficiently preserves vortical structures, (2) eliminates the complexities of mesh generation, (3) is absent of the numerical dissipation associated with mesh-based CFD, (4) does not suffer from the conventional Courant–Friedrichs–Lewy (CFL) condition, and (5) is 100x faster than mesh-based LES with comparable fidelity. Fig. 1 shows a large eddy simulation of an eVTOL aircraft using the reformulated VPM.

In this study, we build upon the meshless LES scheme developed in References [2] and [12] to create a solver for interactional aerodynamics. This poses the challenge of introducing solid boundaries without a mesh. While the reader is referred to our previous work [2] for the derivation of the LES method and subfilter scale model, the focus in this study will be that of developing and validating actuator models that introduce wings and rotating blades in the computational domain.

Large eddy simulation aims at resolving the main structure of the flow, while smaller scales are modeled rather than resolved. Hence, in the proximity of a solid surface, instead of resolving the boundary layer down to the smallest  $y^+$ , solid bodies are often captured through either an immersed boundary method or an actuator model. Common immersed boundary methods introduce a penalization function in the Navier-Stokes equations that mimics the effects of both no-slip and no-flow-through boundary conditions at the surface of the body [13]. Actuator models, on the other hand, calculate and immerse the momentum imparted by the body to the fluid as a force term in the Navier-Stokes equations [14].

In rotor simulations, the simplest actuator model is the *actuator disk model* (ADM) [15, 16]. ADM uses a spatial average of the velocity field at the rotor disk to calculate the force along the blade from airfoil lookup tables. The blade loading is then distributed azimuthally along the rotor disk and introduced in the momentum Navier-Stokes equation as a momentum source. The rotor loads and momentum source terms thus computed by ADM are time averages, which

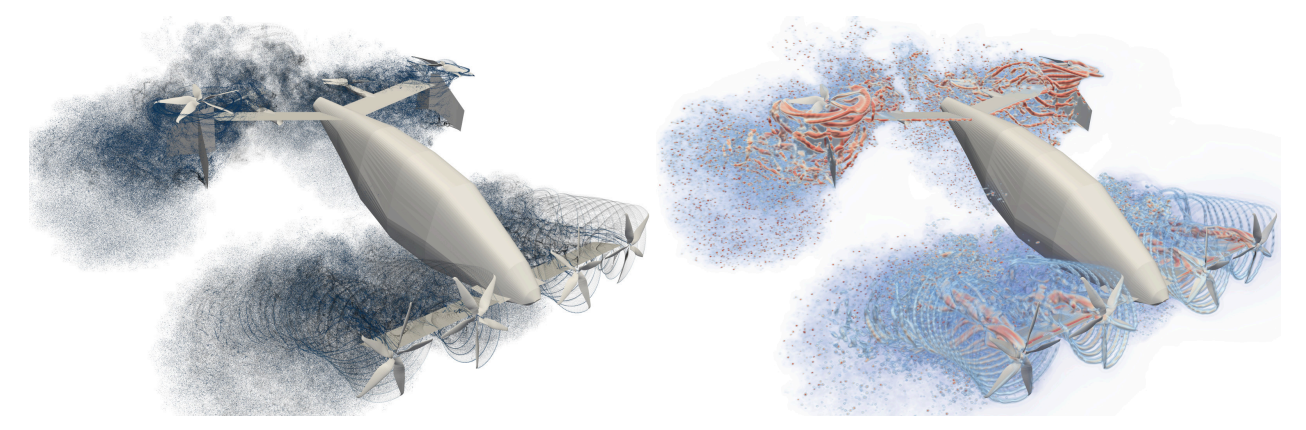


Fig. 1 Meshless LES of multirotor aircraft using the reformulated VPM: (left) computational elements (vortex particles), and (right) volume rendering of vorticity field. Retrieved from the doctoral dissertation [12] accompanying this work.

result in a time-averaged propeller wake. This has the drawback that the predicted wake lacks the tip vortices and unsteady dynamics that drive many interactional aerodynamic phenomena.

A model that is better suited for unsteady simulations is the *actuator line model* (ALM) [17, 18]. ALM calculates the effective angle of attack from the local velocity along each blade as the blades move. Typically, the force is then placed at the aerodynamic center of the airfoil section as a momentum source, thus constructing a lifting line that rotates with the blade. Tip vortices are shed as blades move and the wake is accurately resolved. Studies have shown that wake dynamics and unsteady quantities (like sectional thrust and power) predicted with ALM can be as accurate as a blade-resolved simulation [19, 20].

In like manner to a rotor, ALM may also be used to simulate a fixed wing. In the case of an isolated wing, ALM can lead to an accurate lift and drag distribution as well as resolving the wake. However, when another wake is impinging directly on the surface of the wing (as in the case of a blown wing), ALM can lead to unphysical wing-on-wake interactions, which in turn lead to an inaccurate wing loading. This is because the impinging wake sees the ALM wing only as a lifting line as opposed to a solid surface.

A model that is better suited for wake impingement is the *actuator surface model* (ASM) [21]. Whereas ALM places the force at the aerodynamic center of the airfoil, ASM uses precomputed pressure and skin friction distributions to distribute the force along the airfoil's mean camber line. Thus, the wing is represented as a lifting surface as opposed to a line. Studies have shown that ASM leads to accurate pressure and velocity fields in the proximity of the surface [21–23], which makes ASM a promising approach to capture complex wing-wake interactions as in the case of a blown wing.

Whereas the aforementioned actuator models were originally developed as a momentum-source term for the Navier-Stokes equations in their pressure-velocity form, a different approach is needed for a solver based on the vorticity equation (as in the case of vortex methods). Chatelain et al. [24] proposed introducing the aerodynamic force of an actuator line model into the vorticity equation by immersing the vorticity associated with its circulation. Later work applied this to both horizontal [25] and vertical [26] wind turbines. Caprace et al. [27] expounded on this by defining a "dragging line" to also immerse the vorticity associated with parasitic drag, and applied it to a wing. This lifting and dragging ALM approach was then applied to a rotor in edgewise flight, resolving the wake with unprecedented fidelity [28]. While ALM has been successfully applied to vortex methods, no precedent of an ASM application to vortex methods is found in the literature.

In this study, we further develop our meshless LES scheme to include propellers and wings in the computational domain through actuator models, as explained in Section II. In Section II.C, blades are captured through an actuator line model following well-established practices for LES. In Section II.D, a novel, vorticity-based, actuator surface model is developed for wings, suitable for propeller-wing interactions when a wake impinges on the surface of a wing. This ASM imposes the no-flow-through condition at the airfoil centerline by calculating the circulation that meets this condition and by immersing the associated vorticity following a pressure-like distribution. In order to incrementally validate each aspect of the interactions encountered when a propeller wake impinges on a wing, first, the isolated wing and the isolated propeller are simulated and validated in Section III. Extensive validation of propeller-wing interactions predicted with our meshless LES is then presented in Section IV, simulating both a tailplane with tip-mounted propellers and a wing with propellers mounted mid-span, and comparing our results to experimental measurements found in the literature. The models developed in this study are implemented and integrated with the reformulated VPM code FLOWVPM\* in the open-source solver FLOWUnsteady [29]. †

# II. Modeling Methodology

In this section, we build upon the meshless LES scheme developed in References [2] and [12] to create a solver for interactional aerodynamics. First, the governing equations of the reformulated VPM and the subfilter-scale model that constitute the meshless LES scheme are summarized in Section II.A. Actuator models will be formulated by immersing their vorticity in the vorticity-velocity form of the Navier-Stokes equations, as explained in Section II.B. In Section II.C, an ALM based on tabulated data will be developed for propellers. In Section II.D, an ASM based on a circulation solver will be developed for wings, which will be applied to the case of wake impingement on a blown wing.

<sup>\*</sup>Open-source code available at github.com/byuflowlab/FLOWVPM.jl

<sup>†</sup>Open-source code available at github.com/byuflowlab/FLOWUnsteady

#### A. Meshless Large Eddy Simulation

In recent work [2, 12], we have derived a new formulation of the vortex particle method (VPM) from the LES-filtered Navier-Stokes equations. The new method, referred to as the reformulated VPM or rVPM, is an LES that is both numerically stable and meshless, and is able to accurately resolve mean and fluctuating large-scale features of turbulent flow with minimal computational effort. Hereby we concisely summarize the governing equations of the reformulated VPM, and the reader is referred to Alvarez and Ning [2] and the doctoral dissertation [12] accompanying this work for a detailed derivation of the method.

The reformulated VPM uses a Lagrangian scheme to solve the vorticity form of the LES-filtered Navier-Stokes equations

$$\frac{\partial \overline{\omega_i}}{\partial t} + \overline{u_j} \frac{\partial \overline{\omega_i}}{\partial x_j} = \overline{\omega_j} \frac{\partial \overline{u_i}}{\partial x_j} + \nu \nabla^2 \overline{\omega_i} - \frac{\partial T'_{ij}}{\partial x_j} + \frac{\partial T_{ij}}{\partial x_j}, \tag{1}$$

where the bar denotes the filter operator<sup>‡</sup>, and  $T_{ij} \equiv \overline{u_i \omega_j} - \overline{u_i \omega_j}$  is the subfilter-scale (SFS) vorticity stress capturing the interactions between large-scale dynamics and SFS dynamics. The term  $\partial T'_{ij}/\partial x_j$  represents the SFS contributions arising from the advective term (vorticity advection), while  $\partial T_{ij}/\partial x_j$  represents the contributions arising from vortex stretching. For simplicity, Eq. (1) is written in vector notation as

$$\frac{\mathrm{d}}{\mathrm{d}t}\overline{\omega} = (\overline{\omega}\cdot\nabla)\,\overline{\mathbf{u}} + \nu\nabla^2\overline{\omega} - \mathbf{E}_{\mathrm{adv}} - \mathbf{E}_{\mathrm{str}},\tag{2}$$

where  $(\mathbf{E}_{\mathrm{adv}})_i \equiv \frac{\partial T'_{ij}}{\partial x_j}$  is the SFS vorticity advection,  $(\mathbf{E}_{\mathrm{str}})_i \equiv -\frac{\partial T_{ij}}{\partial x_j}$  is the SFS vortex stretching, and the  $\frac{\mathrm{d}}{\mathrm{d}t}$  operator is the linearized version of the filtered material derivative,  $\frac{\mathrm{d}}{\mathrm{d}t}() \equiv \frac{\partial}{\partial t}() + (\overline{\mathbf{u}} \cdot \nabla)()$ . Notice that casting the Navier-Stokes equation into this vorticity form gets rid of all dependance on pressure. Furthermore, this equation depends on  $\omega$  alone since  $\mathbf{u}$  can be calculated directly from  $\omega$  through the Biot-Savart law.

The material derivative in Eq. (2) and the material-conservative nature of the vorticity makes the  $\omega$  field especially well fit for a Lagrangian description. The unfiltered  $\omega$  field is discretized with singular vortex particles of positions  $\mathbf{x}_p$  and coefficients  $\Gamma_p$  (called *vortex strength*), approximating  $\omega$  as

$$\omega(\mathbf{x},t) \approx \sum_{p} \mathbf{\Gamma}_{p}(t) \delta(\mathbf{x} - \mathbf{x}_{p}(t)),$$
 (3)

where  $\delta$  is the Dirac delta. Applying the filter operator,

$$\overline{\omega}(\mathbf{x}) = \int_{-\infty}^{\infty} \omega(\mathbf{y}) \zeta_{\sigma}(\mathbf{x} - \mathbf{y}) d\mathbf{y} \approx \int_{-\infty}^{\infty} \left( \sum_{P} \mathbf{\Gamma}_{P} \delta(\mathbf{y} - \mathbf{x}_{P}) \right) \zeta_{\sigma}(\mathbf{x} - \mathbf{y}) d\mathbf{y},$$

the Dirac delta collapses the integral, obtaining an approximation of the filtered vorticity field as

$$\overline{\boldsymbol{\omega}}(\mathbf{x},t) \approx \sum_{p} \mathbf{\Gamma}_{p}(t) \zeta_{\sigma_{p}}(\mathbf{x} - \mathbf{x}_{p}(t)), \tag{4}$$

where  $\zeta_{\sigma}(\mathbf{x}) \equiv \frac{1}{\sigma^3} \zeta\left(\frac{\|\mathbf{x}\|}{\sigma}\right)$  is the filter kernel of width  $\sigma$  and radial basis  $\zeta$ . As seen in Eq. (4), the filter operator has the effect of spreading the vortex strength  $\Gamma_p$  in space, regularizing the singularity originally introduced by the Dirac delta. Thus, the filter kernel takes the role of a basis function that is used to discretize  $\overline{\omega}$  through particles. We let the filter width  $\sigma$  (here on called *smoothing radius* or *core size*) change in time and space according to the evolution of each individual particle. The particle field constructs a continuous vorticity field through radial basis functions as given by Eq. (4), and also a continuous velocity field by inverting the relation  $\overline{\omega} = \nabla \times \overline{\mathbf{u}}$  as

$$\overline{\mathbf{u}}\left(\mathbf{x}\right) = -\frac{1}{4\pi} \sum_{p} g_{\sigma_{p}}\left(\mathbf{x} - \mathbf{x}_{p}\right) \frac{\mathbf{x} - \mathbf{x}_{p}}{\|\mathbf{x} - \mathbf{x}_{p}\|^{3}} \times \mathbf{\Gamma}_{p},\tag{5}$$

 $<sup>^{\</sup>ddagger}$ Let  $\phi$  be a field and  $\zeta_{\sigma}$  a filter kernel with cutoff length  $\sigma$ , the filter operator is defined as  $\overline{\phi}(\mathbf{x}) \equiv \int\limits_{-\infty}^{\infty} \phi(\mathbf{y}) \zeta_{\sigma}(\mathbf{x} - \mathbf{y}) \, \mathrm{d}\mathbf{y}$ .

where  $g_{\sigma}$  is the regularizing function [1] associated with the filter kernel  $\zeta_{\sigma}$ . Hence, all fluid properties—like  $\overline{\mathbf{u}}$  and its spatial derivatives—are continuous and can be computed analytically.

Similar to the process that led from Eq. (3) to Eq. (4), we use singular particles to discretize the LES-filtered vorticity equation given in Eq. (2), and arrive to the governing equations of the reformulated VPM:

$$\frac{\mathrm{d}}{\mathrm{d}t}\mathbf{x}_p = \overline{\mathbf{u}}(\mathbf{x}_p) \tag{6}$$

$$\frac{\mathrm{d}}{\mathrm{d}t}\mathbf{\Gamma}_{p} = \left(\mathbf{\Gamma}_{p}\cdot\nabla\right)\mathbf{\overline{u}}(\mathbf{x}_{p}) - \frac{g+f}{\frac{1}{3}+f}\left\{\left[\left(\mathbf{\Gamma}_{p}\cdot\nabla\right)\mathbf{\overline{u}}(\mathbf{x}_{p})\right]\cdot\hat{\mathbf{\Gamma}}_{p}\right\}\hat{\mathbf{\Gamma}}_{p} - \frac{C_{d}}{\zeta_{\sigma_{p}}(\mathbf{0})}\left[\mathbf{E}_{\mathrm{str}}(\mathbf{x}_{p}) - \frac{f}{\frac{1}{3}+f}\left(\mathbf{E}_{\mathrm{str}}(\mathbf{x}_{p})\cdot\hat{\mathbf{\Gamma}}_{p}\right)\hat{\mathbf{\Gamma}}_{p}\right]\right\}$$
(7)

$$\frac{\mathrm{d}}{\mathrm{d}t}\sigma_{p} = -\left(\frac{g+f}{1+3f}\right)\frac{\sigma_{p}}{\|\mathbf{\Gamma}_{p}\|}\left[\left(\mathbf{\Gamma}_{p}\cdot\nabla\right)\overline{\mathbf{u}}(\mathbf{x}_{p})\right]\cdot\hat{\mathbf{\Gamma}}_{p} + \left(\frac{f}{1+3f}\right)\frac{\sigma_{p}}{\|\mathbf{\Gamma}_{p}\|}\frac{C_{d}}{\zeta_{\sigma_{p}}(\mathbf{0})}\mathbf{E}_{\mathrm{str}}(\mathbf{x}_{p})\cdot\hat{\mathbf{\Gamma}}_{p}$$
(8)

$$\left(\frac{\mathrm{d}}{\mathrm{d}t}\overline{\omega}\right)_{\mathrm{viscous}} = \nu\nabla^2\overline{\omega} \tag{9}$$

where Eq. (6) resolves vorticity advection by convecting the particles, Eq. (7) governs the evolution of vortex strength, and Eq. (8) governs the evolution of particle size. Eq. (7) in conjunction with Eqs. (6) and (8) resolve the inviscid part of the LES-filtered vorticity Navier-Stokes equation, while the viscous part in Eq. (9) can be resolved through any of the schemes previously proposed in the literature (*e.g.*, vortex redistribution method [30, 31], particle strength exchange [32], or core spreading [33]). The parameters f and g dictate how vortex stretching is distributed between vortex strength and vortex core size, and their values are derived from the element shape and conservation laws, as explained in References [2] and [12].

The main headway of the reformulated VPM over the classic VPM is that rVPM uses the particle size, or  $\frac{d}{dt}\sigma_p$ , as an extra degree of freedom to reinforce conservation laws. As shown in References [2] and [12], momentum and mass conservation leads to f = 0 and  $g = \frac{1}{5}$ , and Eqs. (7) and (8) become

$$\begin{split} &\frac{\mathrm{d}}{\mathrm{d}t}\boldsymbol{\Gamma}_{p} = \left(\boldsymbol{\Gamma}_{p}\cdot\boldsymbol{\nabla}\right)\overline{\mathbf{u}}(\mathbf{x}_{p}) - \frac{3}{5}\left\{\left[\left(\boldsymbol{\Gamma}_{p}\cdot\boldsymbol{\nabla}\right)\overline{\mathbf{u}}(\mathbf{x}_{p})\right]\cdot\hat{\boldsymbol{\Gamma}}_{p}\right\}\hat{\boldsymbol{\Gamma}}_{p} - \frac{C_{d}}{\zeta_{\sigma_{p}}(\mathbf{0})}\mathbf{E}_{\mathrm{str}}(\mathbf{x}_{p})\\ &\frac{\mathrm{d}}{\mathrm{d}t}\sigma_{p} = -\frac{1}{5}\frac{\sigma_{p}}{\|\boldsymbol{\Gamma}_{p}\|}\left[\left(\boldsymbol{\Gamma}_{p}\cdot\boldsymbol{\nabla}\right)\overline{\mathbf{u}}(\mathbf{x}_{p})\right]\cdot\hat{\boldsymbol{\Gamma}}_{p}, \end{split}$$

which is the formulation referred to as the "reformulated VPM". Notice that when f=g=0 and  $\mathbf{E}_{\mathrm{str}}$  is neglected, Eqs. (7) and (8) collapse back to the classic VPM equations, making these equations a generalization of the classic method. In Reference [12], we show that the classic VPM turns out to violate both conservation of momentum and mass when it assumes  $\frac{\mathrm{d}}{\mathrm{d}t}\sigma_p=0$ , which explains the tendency of the classic VPM to be numerically unstable. Furthermore, notice that the rVPM equations do not require more computation than the classic VPM: when SFS effects are neglected ( $\mathbf{E}_{\mathrm{str}}=0$ ), both  $\frac{\mathrm{d}\sigma_p}{\mathrm{d}t}$  and  $\frac{\mathrm{d}\Gamma_p}{\mathrm{d}t}$  are calculated directly and solely from vortex stretching,  $(\Gamma_p\cdot\nabla)\,\bar{\mathbf{u}}(\mathbf{x}_p)$ . Turning our attention back to the SFS stress tensor  $T_{ij}$ , the accuracy of LES hinges on the modeling of this tensor. Its

Turning our attention back to the SFS stress tensor  $T_{ij}$ , the accuracy of LES hinges on the modeling of this tensor. Its divergence represents the rate at which enstrophy—a measure of rotational kinetic energy—is transferred from resolved scales to subfilter scales (diffusion) and from subfilter scales to resolved scales (backscatter). In vortex methods, the most common SFS models use variants of the Smagorinsky eddy-viscosity model formulated for the vorticity stress [34, 35]. However, these models are developed on the basis of homogeneous isotropic turbulence, which makes them overly diffusive in simulations with coherent vortical structures. In Reference [2], we have developed the following anisotropic model of SFS vortex stretching:

$$\mathbf{E}_{\mathrm{str}}\left(\mathbf{x}\right) \approx \sum_{q} \zeta_{\sigma}(\mathbf{x} - \mathbf{x}_{q}) \left(\mathbf{\Gamma}_{q} \cdot \nabla\right) \left(\overline{\mathbf{u}}\left(\mathbf{x}\right) - \overline{\mathbf{u}}\left(\mathbf{x}_{q}\right)\right).$$

The model coefficient  $C_d$  is calculated dynamically at the position of every particle as

$$C_d = \frac{\left\langle \mathbf{\Gamma}_p \cdot \mathbf{L} \right\rangle}{\left\langle \mathbf{\Gamma}_p \cdot \mathbf{m} \right\rangle},$$

where  $\langle \cdot \rangle$  denotes an integration along Lagrangian trajectories [36], and

$$\mathbf{m} = \frac{\sigma^3}{\zeta(0)} \frac{\partial \mathbf{E}_{\text{str}}}{\partial \sigma} (\mathbf{x}_p)$$

$$\mathbf{L} = \frac{3}{\sigma} (\mathbf{\Gamma}_p \cdot \nabla) (\mathbf{u}(\mathbf{x}_p) - \overline{\mathbf{u}}(\mathbf{x}_p)) + (\mathbf{\Gamma}_p \cdot \nabla) \frac{\partial \overline{\mathbf{u}}}{\partial \sigma} (\mathbf{x}_p).$$

This dynamic procedure is based on a simultaneous balance of enstrophy-production and derivatives between true and modeled SFS contributions. Backscatter is controlled by clipping the model coefficient to  $C_d = 0$  whenever the condition  $C_d \Gamma_p \cdot \mathbf{E}_{\text{str}}(\mathbf{x}_p) \ge 0$  is not satisfied. This results in a low-dissipation SFS model that uses vortex stretching as the physical mechanism for turbulence, which is well suited for flows with coherent vortical structures where the predominant cascade mechanism is vortex stretching.

In this study, vortex stretching is resolved with the transposed scheme [1, 37] and the divergence of the vorticity field is treated through the relaxation scheme developed by Pedrizzeti [38]. The time integration of the governing equations is done through a low-storage third-order Runge-Kutta scheme [39]. A Gaussian kernel is used as the LES filter  $\zeta_{\sigma}$  (or VPM radial basis function). Like the classic VPM, the reformulated VPM is spatially second-order accurate in the convective term when a Gaussian basis is used [40]. Viscous diffusion is solved through the core spreading method coupled with the radial basis function interpolation approach for spatial adaptation developed by Barba [41–43]. This viscous scheme has second-order spatial convergence, while showing linear convergence when coupled with spatial adaptation [33]. The fast multipole method [44, 45] (FMM) is used for the computation of the regularized Biot-Savart law, approximating the velocity field and vortex stretching through spherical harmonics with computational complexity O(N), where N is the number of particles. The FMM computation of vortex stretching is performed through an efficient complex-step derivative approximation [46], implemented in a modified version of the open-source, parallelized code ExaFMM [47, 48]. FLOWVPM and FLOWUnsteady are implemented in the Julia language [49], which is a modern, high-level, dynamic programming language for high-performance computing.

# **B.** Meshless LES With Immersed Vorticity

In order to immerse the vorticity of solid boundaries into the LES-filtered Navier-Stokes equations, the filtered vorticity field  $\overline{\omega}(\mathbf{x},t)$  is decomposed into a free-vorticity field  $\overline{\omega}_{\text{free}}(\mathbf{x},t)$  and a bound-vorticity field  $\overline{\omega}_{\text{bound}}(\mathbf{x},t)$  as

$$\overline{\omega} = \overline{\omega}_{\text{free}} + \overline{\omega}_{\text{bound}}$$
.

Both components can be discretized with vortex particles as

$$\overline{\omega}(\mathbf{x}) = \underbrace{\sum_{p} \Gamma_{p} \zeta_{\sigma_{p}} (\mathbf{x} - \mathbf{x}_{p})}_{\overline{\omega}_{\text{free}}} + \underbrace{\sum_{b} \Gamma_{b} \zeta_{\sigma_{b}} (\mathbf{x} - \mathbf{x}_{b})}_{\overline{\omega}_{\text{bound}}},$$

where the particles discretizing the free-vorticity field evolve according to the rVPM governing equations, Eqs. (6) to (9), while the ones discretizing the bound-vorticity are embedded on the solid boundaries and their strength is calculated by actuator models derived in Sections II.C and II.D. The velocity field is obtained by inverting the relation  $\omega = \nabla \times \mathbf{u}$ , resulting in

$$\overline{\mathbf{u}}\left(\mathbf{x}\right) = \underbrace{\sum_{p} g_{\sigma_{p}}\left(\mathbf{x} - \mathbf{x}_{p}\right) \mathbf{K}\left(\mathbf{x} - \mathbf{x}_{p}\right) \times \mathbf{\Gamma}_{p}}_{\overline{\mathbf{u}}_{\text{free}}} + \underbrace{\sum_{b} g_{\sigma_{b}}\left(\mathbf{x} - \mathbf{x}_{b}\right) \mathbf{K}\left(\mathbf{x} - \mathbf{x}_{b}\right) \times \mathbf{\Gamma}_{b}}_{\overline{\mathbf{u}}_{\text{bound}}},$$

which includes the velocity induced by both free and bound vorticity components, and where  $\mathbf{K}(\mathbf{x}) \equiv -\frac{1}{4\pi} \frac{\mathbf{x}}{\|\mathbf{x}\|^3}$ . Thus, the evolution of the free particles is influenced by the vorticity immersed at the solid boundaries, affecting their convection and vortex stretching through the velocity field induced by the bound particles.

The immersed vorticity not only affects the evolution of existing free vorticity, but it also creates new free vorticity at the boundary through viscous diffusion. In reality, vorticity is created in the boundary layer, it builds up as it travels along the surface, and it is eventually shed off the surface either by the Kutta condition at the trailing edge, flow separation, or other turbulent mechanisms. On a slender body, the vorticity can be assumed to be shed at the trailing edge.

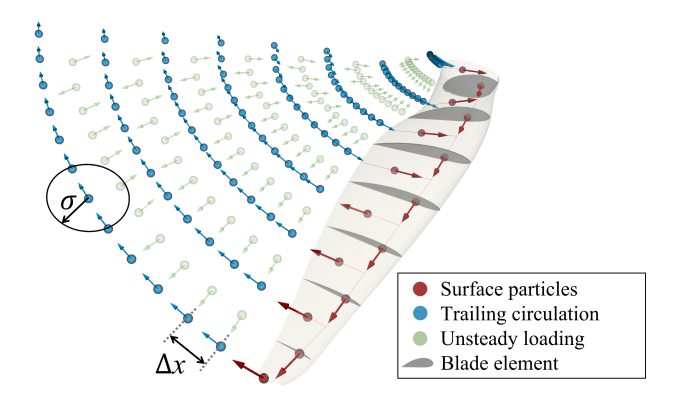


Fig. 2 Particles used for immersed vorticity in actuator line model. Particles colored by their source of vorticity; arrows indicate direction of vortex strength. Figure reproduced from Alvarez and Ning [46].

In our simulations, instead of creating vorticity through the viscous diffusion equation, the immersed vorticity is shed along a prescribed trailing edge. This approach neglects the wake created by flow separation. However, the effects of flow separation on loading (like the drop in lift and increase in pressure drag on a stalled airfoil) can still be captured whenever lookup airfoil tables are used.

# C. Propeller Model (Actuator Line Model)

Propellers will be introduced in our meshless LES through an actuator line model (ALM). Studies have shown that wake dynamics and unsteady quantities (like thrust and power) predicted with ALM can be as accurate as a blade-resolved simulation [19, 20]. Actuator models typically include two schemes: one scheme for calculating blade forces from the fluid domain, and another scheme for immersing such forces back into the fluid domain. Blade forces are calculated in our ALM using blade elements with lookup airfoil tables, as explained in References [46] and [12], which is a common ALM approach.

Instead of introducing the force as a momentum source as typically done in conventional CFD, the force is introduced in our meshless LES by immersing its associated vorticity. The aerodynamic loading is first converted into a circulation distribution  $\Gamma$  using the Kutta-Joukowski theorem as

$$\Gamma = \frac{cV_{\text{local}}}{2}c_{\ell},$$

where  $V_{local}$  is the local velocity seen by the blade element, c is its chord length, and  $c_{\ell}$  is the lift coefficient calculated by the blade element. The vorticity is immersed by embedding particles along the surface that capture the blade's circulation distribution, while shedding free particles at the trailing edge associated with unsteady loading and trailing circulation, as shown in Fig. 2.

# D. Wing Model (Actuator Surface Model)

While an ALM based on tabulated airfoil data is accurate for propellers, such an actuator model is only loosely-coupled with the fluid domain and imposes no boundary conditions. This makes it inadequate for cases with strong wake impingement on a surface, as in the case of a blown wing. Hence, wings will be introduced in our meshless LES through a different actuator model that is tightly coupled imposing a boundary condition at the surface of the wing. This boundary condition, called *no-flow-through condition*, consists of imposing a zero velocity normal to the surface of the wing, meaning that no flow goes through the surface. In this section we show how (1) the boundary conditions is satisfied solving for the circulation distribution that cancels the normal flow, (2) the associated vorticity is immersed in the LES, and (3) the forces on the wing are calculated.

## 1. Circulation Solver

The wing is discretized into wing elements in similitude to the discrete-vortex Weissinger model [50], as shown in Fig. 3. Each wing element is composed of a bound vortex at the quarter-chord position (line  $\overline{AB}$ ) and two trailing

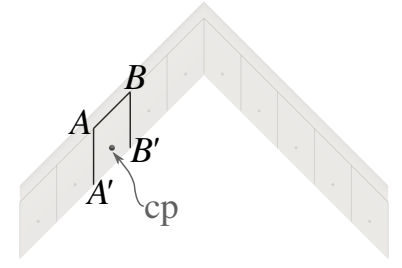


Fig. 3 Wing element used in circulation solver.

bound vortices extending to the trailing edge (lines  $\overline{A'A}$  and  $\overline{BB'}$ ). The velocity induced by the *i*-th wing element is approximated through vortex filaments as

$$\mathbf{u}_{i}(\mathbf{x}) = \Gamma_{i} \sum_{(a,b) \in \mathbb{H}_{i}} \mathbf{g}_{ab}(\mathbf{x}), \qquad \mathbb{H}_{i} = \{(A',A), (A,B), (B,B')\},$$

where

$$\mathbf{g}_{ab}(\mathbf{x}) = \frac{1}{4\pi} \frac{\mathbf{r}_a \times \mathbf{r}_b}{\|\mathbf{r}_a \times \mathbf{r}_b\|^2} \left( \frac{\mathbf{r}_a}{\|\mathbf{r}_a\|} - \frac{\mathbf{r}_b}{\|\mathbf{r}_b\|} \right) \cdot \mathbf{r}_{ab},$$

 $\mathbf{r}_{ab} = \mathbf{x}_b - \mathbf{x}_a$ ,  $\mathbf{r}_a = \mathbf{x} - \mathbf{x}_a$ , and  $\mathbf{r}_b = \mathbf{x} - \mathbf{x}_b$ . For ease of notation, we rewrite this as

$$\mathbf{u}_{i}\left(\mathbf{x}\right) = \Gamma_{i}\mathbf{G}_{i}(\mathbf{x})\tag{10}$$

where  $G_i \equiv \sum g_{ab}$  contains the geometric information of the *i*-th wing element. The wing's self-induced velocity is then calculated iterating over each element as

$$\mathbf{u}_{\text{wing}}\left(\mathbf{x}\right) = \sum_{i} \mathbf{u}_{i}\left(\mathbf{x}\right). \tag{11}$$

In order to compute the circulation  $\Gamma$  along the wing, a control point  $\mathbf{x}_{cp}$  is defined at the three-quarter-chord position of each wing element shown in Fig. 3, on which the no-flow-through condition is imposed. A local velocity  $\mathbf{u}_{local}$  is calculated by adding the wing-induced velocity  $\mathbf{u}_{wing}$ , the kinematic velocity due to the motion of the wing  $\mathbf{u}_{kin}$ , and the velocity field computed by the LES  $\mathbf{u}_{LES}$  (calculated before immersing the vorticity of the wing surface§). The local velocity at the *i*-th control point is then computed as

$$\mathbf{u}_{\text{local}}^{i}(t) = \mathbf{u}_{\text{wing}}(\mathbf{x}_{\text{cp}}^{i}, t) + \mathbf{u}_{\text{kin}}^{i}(t) + \mathbf{u}_{\text{LES}}(\mathbf{x}_{\text{cp}}^{i}, t)$$

and the no-flow-through condition is imposed as

$$\mathbf{u}_{\text{local}}^i \cdot \hat{\mathbf{n}}_i = 0,$$

leading to

$$\mathbf{u}_{\text{wing}}^{i} \cdot \hat{\mathbf{n}}_{i} = -\left(\mathbf{u}_{\text{kin}}^{i} + \mathbf{u}_{\text{LFS}}^{i}\right) \cdot \hat{\mathbf{n}}_{i},\tag{12}$$

where the superscript *i* denotes the corresponding function evaluated at the *i*-th control point, and  $\hat{\mathbf{n}}_i$  is the unit vector that represents the normal to the surface at the *i*-th element. We approximate  $\hat{\mathbf{n}}$  as  $\mathbf{n} = (\mathbf{x}_{A'} - \mathbf{x}_A) \times (\mathbf{x}_B - \mathbf{x}_A)$  and  $\hat{\mathbf{n}} = \mathbf{n}/\|\mathbf{n}\|$ .

Replacing Eqs. (10) and (11) in Eq. (12), we arrive to

$$\sum_{i} \Gamma_{j} \mathbf{G}_{j}^{i} \cdot \hat{\mathbf{n}}_{i} = -\left(\mathbf{u}_{\text{kin}}^{i} + \mathbf{u}_{\text{LES}}^{i}\right) \cdot \hat{\mathbf{n}}_{i}.$$

<sup>§</sup>Thus, uLES at this point includes the velocity induced by the wing wake, but it excludes the velocity induced by the wing surface on itself.

Given a wing with N elements, this poses a linear system of N equations (one for each control point  $\mathbf{x}_{cp}^i$ ) and N unknowns,  $\Gamma_j$ . The circulation distribution  $\Gamma_j$  that satisfies the boundary condition is then obtained by solving the system of equations.

When the vorticity of the wing is immersed in the fluid domain, the LES solver and the circulation solver become tightly coupled. We have observed that this system can become numerically unstable when the wing experiences large velocity fluctuations, hence we introduce a relaxation procedure that updates  $\Gamma$  as

$$\Gamma_{\text{new}} = \alpha \Gamma + (1 - \alpha) \Gamma_{\text{old}}$$
.

All simulations in this study use  $\alpha = 0.3$ .

### 2. Immersed Vorticity

In order to immerse the solid wing surface in the LES, the vorticity associated with the circulation distribution needs to be spread chordwise rather than concentrated at the lifting line. This requires assuming a distribution  $g(x^*)$  that will spread the circulation of the *i*-th blade element into a vortex sheet of strength  $\gamma(x^*)$  as

$$\gamma(x^*) = \Gamma_i g(x^*), \quad \text{with } \int_{-\infty}^{\infty} g(x/c) \, \mathrm{d}x = 1$$

and where  $x^* = x/c$  is the chordwise position. At the same time, the trailing circulation is spread onto a vortex sheet of strength  $\gamma_t(x^*)$  as

$$\gamma_t(x^*) = \int_0^{x^*} \gamma(s) \, \mathrm{d}s,$$

in order to satisfy Kelvin's theorem. Given  $g(x^*)$ , the center of pressure is the centroid of the distribution.

For the sake of simplicity, one may naively assume either a singular or uniform distribution, as shown in Fig. 4 (top and bottom left). The singular distribution turns out to be equivalent to a lifting line rather than a surface, hence, it is not further discussed. The uniform distribution places the center of pressure at x/c = 0.5. An educated guess is that a good ASM would result, in most cases, in a center of pressure close to x/c = 0.25. Hence, the uniform distribution may lead to unphysical results.

Kim et al. [51] suggested using a piecewise linear distribution of the form

$$g(x^*) = \begin{cases} 0.4 + 3.04 \frac{x^*}{0.25} & \text{if } 0 \le x^* < 0.25\\ 3.44 - 3.2 \left(\frac{x^*}{0.25} - 1\right) & \text{if } 0.25 \le x^* < 0.5\\ 0.24 - 0.24 \left(\frac{x^*}{0.5} - 1\right) & \text{if } 0.5 \le x^* \le 1\\ 0 & \text{else} \end{cases}$$

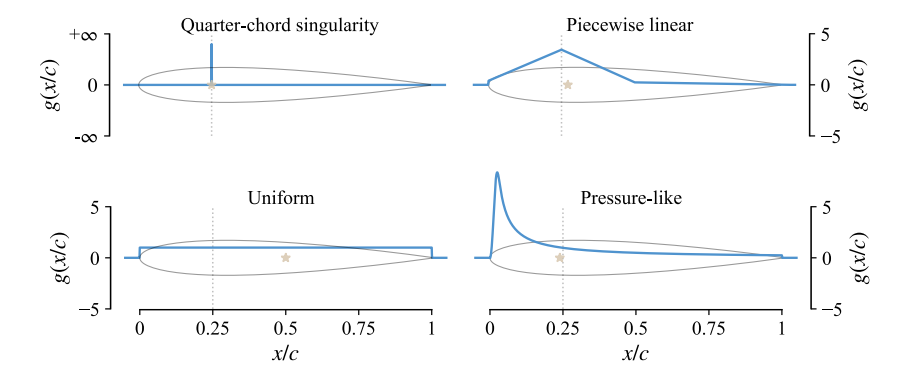


Fig. 4 Vorticity distributions for actuator surface model. Star (★) indicates center of pressure.

which, as shown in Fig. 4 (top right), leads to a center of pressure x/c = 0.27. The ASM distribution by Kim et al. seems somewhat arbitrary, but it has been used for blade-vortex interactions obtaining favorable results [23]. However, this ASM distribution was developed for a momentum source in the pressure-velocity Navier-Stokes equation, and it is not evident that the same distribution should be applied for an immersed vorticity in the vorticity Navier-Stokes equation.

Noticing that most of the turning of the flow is usually done towards the leading edge, and that the pressure distribution typically follows that trend, we now propose a vorticity distribution akin to a pressure distribution. As a reference, Fig. 5 (left) shows the pressure difference between upper and lower surfaces at multiple stations measured experimentally by Veldhuis [52] on a planar wing. Even though the chordwise pressure distribution seems to vary between the different spanwise stations, normalizing each distribution evidences their similarity, as shown in Fig. 5 (right, black lines). Also, note that the center of pressure ranges between x/c = 0.20 to x/c = 0.25. We propose a pressure-like distribution given by

$$g(x^*) = \begin{cases} \frac{a}{4\pi} \frac{1 - \exp\left(-\left(\frac{x^*}{0.02}\right)^3\right)}{x^*} & \text{if } 0 \le x^* \le 1\\ 0 & \text{else} \end{cases}$$

where a is determined numerically as a = 3.061661 in order to obtain a unitary distribution. This distribution is shown in Fig. 5 (right, blue solid line), with its center of pressure at x/c = 0.2393. Fig. 6 shows the simulation of a planar wing (aspect ratio 5.33 and 4° angle of attack) using the pressure-like vorticity distribution, where the vorticity is concentrated at the leading edge, while varying spanwise and chordwise.

In order to assess the fitness of each vorticity distribution, Fig. 7 shows a slice of the flow field around the planar wing with each distribution. The figures in the right show the resulting velocity field and streamlines. The uniform distribution leads to somewhat of a uniform velocity field, which seems unphysical. The piecewise linear distribution

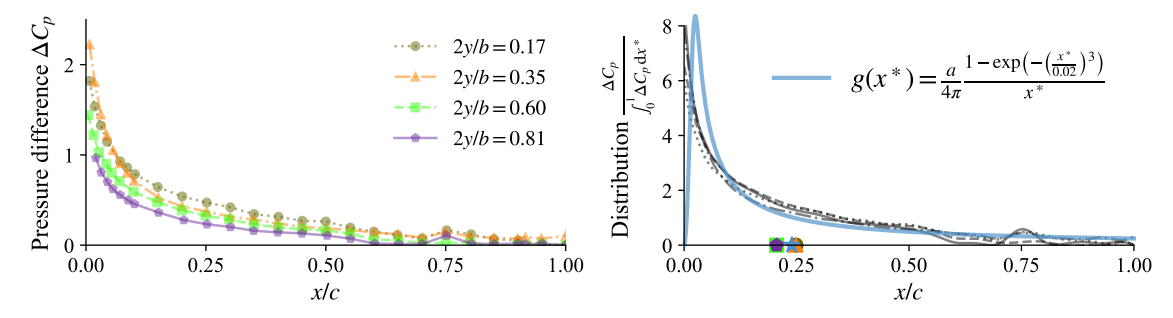


Fig. 5 (left) Experimental chordwise pressure distribution on a planar wing reported by Veldhuis [52], and (right) their normalized distributions. Markers in (right) indicate corresponding centers of pressure.

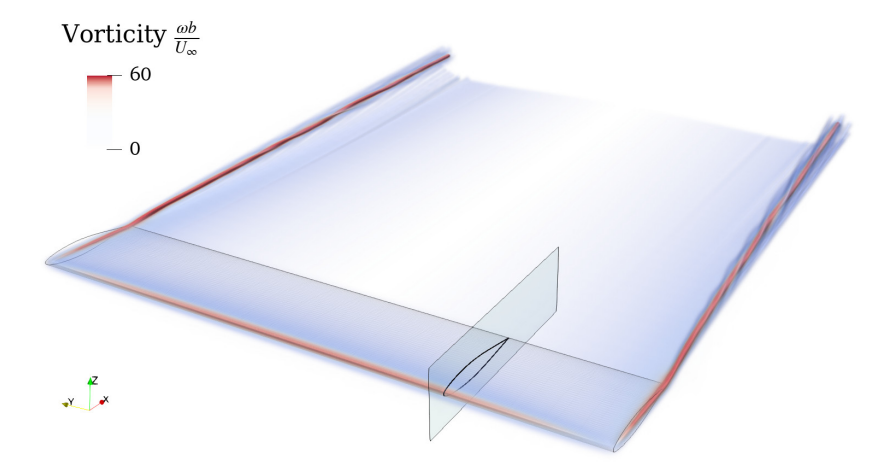
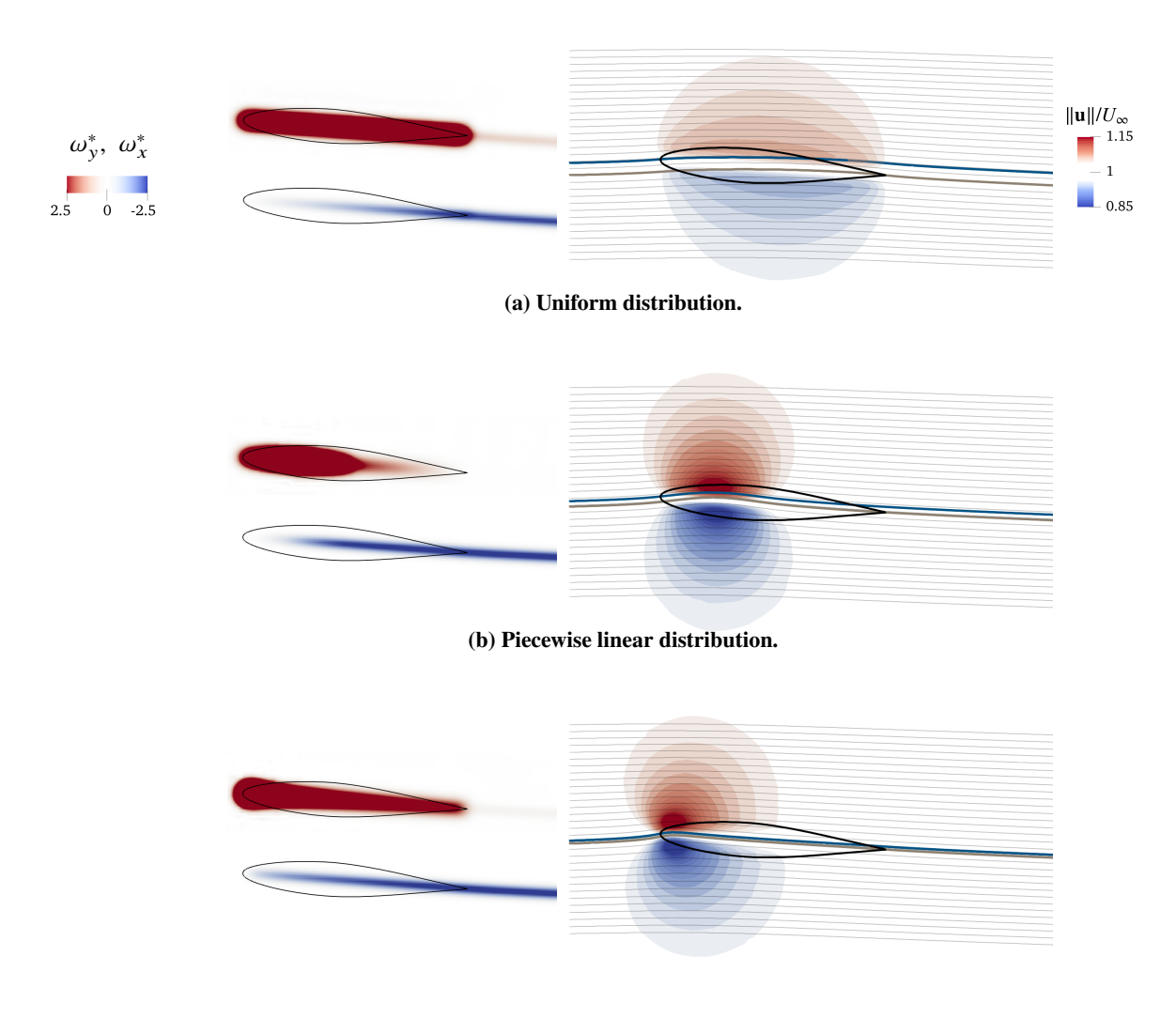


Fig. 6 Wing simulation using ASM with pressure-like distribution. Volume rendering of vorticity magnitude. Vertical plane at 2y/b = 0.5 corresponds to slice shown in Fig. 7.



(c) Pressure-like distribution.

Fig. 7 Slice at 2y/b = 0.5 in planar wing simulation using ASM with different vorticity distributions. (Left) lifting vorticity  $\omega_y^* = \omega_y b/U_\infty$  and trailing vorticity  $\omega_x^* = \omega_x b/U_\infty$ , and (right) velocity magnitude and streamlines. Streamlines that pass through leading edge and trailing edge are shown in blue ( $\blacksquare$ ) and brown ( $\blacksquare$ ), respectively.

leads to a velocity centered at the quarter-chord. The pressure-like distribution leads to a flow that is being turned close to the leading edge, as we hoped for. Note that they all succeed at making the flow tangent to the airfoil centerline at the three-quarter chord position, but there is still some amount of flow going through the centerline surface elsewhere. The streamlines passing through leading and trailing edges are shown in blue and brown, respectively, and the gap between them corresponds to the flow that crosses the centerline. Out of the three distributions, the pressure-like ASM minimizes the amount of flow permeated through the centerline surface, hence this distribution will be used for all simulations in this study.

A pressure-like ASM was previously proposed by Shen et al. [21]; however, their ASM was based on tabulated airfoil data and developed as a momentum-source term for the Navier-Stokes equations in their pressure-velocity form. The novelty of our ASM lays on that it is based on a circulation solver and developed for immersing vorticity in the vorticity form of the Navier-Stokes equations.

In this study, we will prescribe the pressure-like distribution, but future work could improve the ASM by changing

the pressure-like distribution according to angle of attack, airfoil thickness, and camber as suggested by Shen et al. [21], as well as sweep and aspect ratio of the wing. Further improvements can also include distributing the vorticity along the mean camber line as opposed to a straight line between leading and trailing edges, as well as developing a skin-friction-like distribution to immerse and shed the vorticity associated with viscous drag.

#### 3. Force Calculation

The force on the wing is calculated from three components: an aerodynamic force, a viscous force, and an unsteady-circulation force. The aerodynamic force is derived from the turning of the flow around the wing, which yields a version of the Kutta-Joukowski theorem that is suitable for vortex particles as follows.

The intensive force **f** exerted on a fluid, or force per unit volume, is defined as

$$\mathbf{f} = \frac{\mathrm{d}}{\mathrm{d}t} \left( \rho \mathbf{u} \right),$$

which in incompressible flow becomes

$$\mathbf{f} = \rho \frac{\mathrm{d}\mathbf{u}}{\mathrm{d}t}.$$

Expanding the total derivative operator,

$$\mathbf{f} = \rho \frac{\partial \mathbf{u}}{\partial t} + \rho (\mathbf{u} \cdot \nabla) \mathbf{u},$$

we notice that this is simply the left-hand side of the Navier-Stokes momentum equation. The force can then be decomposed into an unsteady component  $\mathbf{f}_{\mathbf{u}} \equiv \rho \frac{\partial \mathbf{u}}{\partial t}$  and a quasi-steady component  $\mathbf{f}_{\mathbf{s}} \equiv \rho (\mathbf{u} \cdot \nabla) \mathbf{u}$  as

$$\mathbf{f} = \mathbf{f}_{\mathrm{u}} + \mathbf{f}_{\mathrm{s}}$$
.

Using the identity  $\nabla(\mathbf{A} \cdot \mathbf{B}) = (\mathbf{A} \cdot \nabla)\mathbf{B} + (\mathbf{B} \cdot \nabla)\mathbf{A} + \mathbf{A} \times (\nabla \times \mathbf{B}) + \mathbf{B} \times (\nabla \times \mathbf{A})$ , the quasi-steady component becomes

$$\mathbf{f}_{s} = \rho \left[ \frac{1}{2} \nabla \left( \mathbf{u} \cdot \mathbf{u} \right) - \mathbf{u} \times (\nabla \times \mathbf{u}) \right].$$

For ease of notation, we write this as

$$\mathbf{f}_{s} = \rho \frac{\nabla \mathbf{u}^{2}}{2} - \rho \mathbf{u} \times \boldsymbol{\omega},$$

where  $\nabla \mathbf{u}^2 \equiv \nabla (\mathbf{u} \cdot \mathbf{u})$  and  $\boldsymbol{\omega} \equiv \nabla \times \mathbf{u}$ . We further decompose the steady force into a kinetic component  $\mathbf{f}_{kin} \equiv \rho \frac{\nabla \mathbf{u}^2}{2}$  and an aerodynamic component  $\mathbf{f}_{aero} \equiv -\rho \mathbf{u} \times \boldsymbol{\omega}$  as

$$\mathbf{f}_{s} = \mathbf{f}_{kin} + \mathbf{f}_{aero}$$
.

Note that  $\mathbf{f}_{aero}$  is the Lamb vector when the density is unitary.

Consider a chunk of fluid with volume Vol, represented by a vortex particle placed at  $\mathbf{x}_p$  inside the volume and vortex strength

$$\Gamma_p \approx \int_{\text{Vol}} \omega \, \mathrm{d}\mathbf{x}.$$

We integrate the aerodynamic component of the intensive force,  $\mathbf{f}_{aero}$ , to get an extensive force in such volume of fluid, denoted  $\mathbf{F}_{aero}$ , as

$$\mathbf{F}_{\text{aero}} = -\rho \int_{\text{Vol}} \mathbf{u}(\mathbf{x}') \times \boldsymbol{\omega}(\mathbf{x}') \, d\mathbf{x}',$$

where we have assumed a uniform density  $\rho$  and incompressible flow. Assuming that the particle is the only source of vorticity inside the volume and using the singular particle approximation,  $\omega(\mathbf{x}) \approx \Gamma_p \delta(\mathbf{x} - \mathbf{x}_p)$ , the force is then approximated as

$$\mathbf{F}_{\text{aero}} \approx -\rho \int_{\mathbf{Vol}} \mathbf{u}(\mathbf{x}') \times \mathbf{\Gamma}_p \delta(\mathbf{x}' - \mathbf{x}_p) d\mathbf{x}',$$

becoming

$$\mathbf{F}_{\text{aero}} \approx -\rho \mathbf{u}(\mathbf{x}_p) \times \mathbf{\Gamma}_p. \tag{13}$$

Thus, we have arrived to a simple but general expression that approximates the aerodynamic force experienced by the fluid. We have chosen to call it "aerodynamic" force since it is caused by the vorticity in the fluid, typically associated with the presence of circulation. Furthermore, the Kutta-Joukowski theorem—the fundamental theorem of aerodynamics—can be derived directly from this expression, as follows.

Suppose that the vorticity in such volume corresponds to the immersed vorticity of a lifting line segment with length  $\ell$  and circulation  $\Gamma$ . The vorticity can then be represented with a bound particle of vortex strength  $\Gamma_b = \Gamma \ell$  placed at the center of the lifting line,  $\mathbf{x}_b$ . The force experienced by the volume of fluid is then

$$\mathbf{F}_{\text{aero}} \approx -\rho \mathbf{u}(\mathbf{x}_b) \times \Gamma \boldsymbol{\ell}$$
.

Since the lifting line corresponds to a wing section, this  $\mathbf{F}_{aero}$  is an external force exerted by the wing on the fluid, and the wing feels the opposite force in response. We denote the force experienced by the wing as  $\mathbf{F}_{kj}$ , defined as

$$\mathbf{F}_{kj} = \rho \mathbf{u}(\mathbf{x}_b) \times \Gamma \boldsymbol{\ell}. \tag{14}$$

If  $\mathbf{u}(\mathbf{x}_b)$  and  $\boldsymbol{\ell}$  are perpendicular, the force per unit length, defined as  $F'_{kj} \equiv \|\mathbf{F}_{kj}\|/\|\boldsymbol{\ell}\|$ , becomes

$$F'_{ki} = \rho u(\mathbf{x}_b) \Gamma,$$

which is the Kutta-Joukowski theorem when  $u(\mathbf{x}_b) = u_{\infty}$ . Hence, the particle approximation of the aerodynamic force given in Eq. (13) is consistent with the theorem.

In the case of the wing section, the velocity field  $\mathbf{u}$  used in Eq. (14) can be the superposition of a freestream  $\mathbf{u}_{\infty}$ , a kinematic velocity  $\mathbf{u}_{kin}$ , the velocity induced by other lifting surfaces  $\mathbf{u}_{wing/blade}$ , and/or a wake velocity  $\mathbf{u}_{wake}$ . In simple terms, the force given by Eq. (14) is the reaction due to the wing section turning the local flow around it. Hence, we refer to this force as the *Kutta-Joukowski force*,  $\mathbf{F}_{kj}$ . Decomposing  $\mathbf{u}$  as

$$u = u_{kin} + \underbrace{u_{\infty} + u_{wing/blade} + u_{wake}}_{u_{LFS}},$$

the last three velocity components are calculated by the LES. Writting  $\Gamma_b = \Gamma \ell$ , the Kutta-Joukowski force is then computed as

$$\mathbf{F}_{kj} = \rho \mathbf{u}_{kin}^b \times \mathbf{\Gamma}_b + \rho \mathbf{u}_{LES}(\mathbf{x}_b) \times \mathbf{\Gamma}_b, \tag{15}$$

which includes lift and induced drag.

Parasitic drag along the wing is calculated using a lookup airfoil table. The drag coefficient  $c_d$  can be determined either from the local angle of attack or the local lift coefficient,  $c_\ell = \frac{2\Gamma}{U_\infty c}$ . Our experience is that the most accurate results are obtained through the local lift coefficient. The parasitic drag includes both form and skin friction drag, where form drag includes both wave drag and pressure drag due to separation.

An additional force term  $F_{\text{uns}}$  is added due to the unsteady changes of circulation, which is calculated as

$$\mathbf{F}_{\text{uns}} = \rho \frac{\mathrm{d}\Gamma}{\mathrm{d}t} A \hat{\mathbf{n}},$$

where A is the area of the wing element and  $\hat{\mathbf{n}}$  is its normal vector.

# **III. Preliminary Validation**

In order to incrementally validate each aspect of the interactions encountered when a propeller wake impinges on a wing, we start by simulating the wing and the propeller in isolation. First, the wing loading predicted with the actuator surface model on a swept-back wing is compared to experimental measurements. Next, we validate the predicted aerodynamic performance of the propeller at an incidence angle. Predicting accurate propeller-wing interactions hinges on accurately resolving the propeller wake. Hence, the vortical structure and velocity in the propeller wake is also validated by comparison to experimental measurements.

# A. Isolated Wing

In order to validate the actuator surface model developed in Section II.D, a  $45^{\circ}$  swept-back wing was simulated following the experiment by Weber and Brebner [53]. This wing has an aspect ratio of 4.9, a span of 2.5 m, an RAE 101 airfoil section with 12% thickness, no dihedral, twist, nor taper, and the high sweep of the wing causes a non-negligible spanwise flow. The freestream velocity  $V_{\infty}$  was 49.7 m/s throughout the tests, corresponding to a chord-based Reynolds number of  $1.7 \times 10^6$ . The wing loads reported by Weber and Brebner were obtained from pressure-tap measurements, hence the drag reported in this section includes induced and form drag while excluding skin friction drag. The simulation

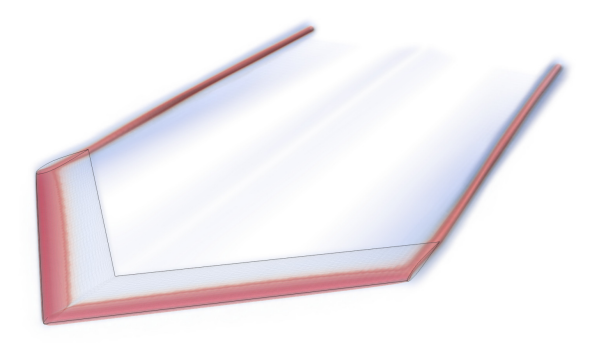


Fig. 8 Simulation of swept-back wing with actuator surface model. Volume rendering of vorticity field.

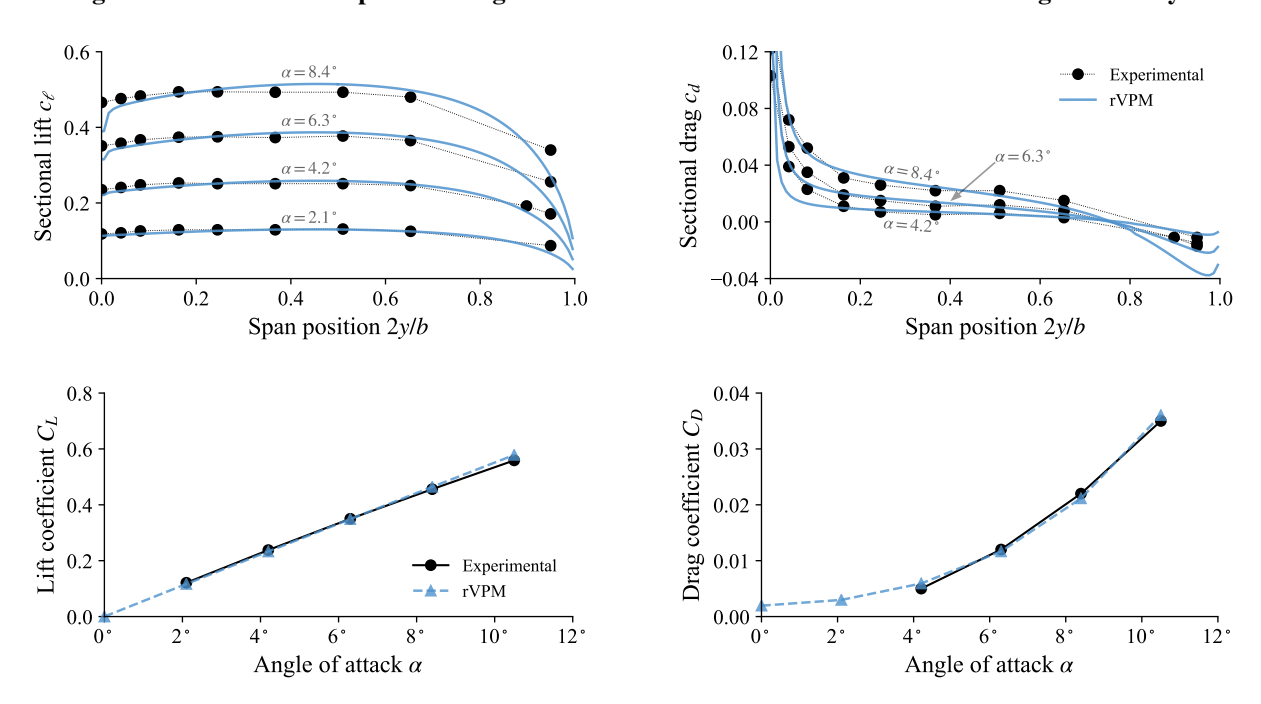


Fig. 9 Spanwise loading distribution (top) and integrated lift and drag (bottom) in swept wing across angle of attack compared to experiment by Weber and Brebner [53].

at an angle of attack (AOA) of 4.2° is shown in Fig. 8, where the vorticity of the actuator surface model is seen to form a vortex sheet along the span, which forms the wing wake as it is shed into the flow field.

Fig. 9 shows the loading distribution and integrated lift and drag across AOA predicted with the actuator surface model, compared to the experimental measurements. The loading distribution shows satisfactory agreement with the experiment, validating that both the circulation solver and the force calculation developed in Section II.D are accurate for predicting not only lift but also drag distribution across the span. The integrated lift and drag (Fig. 9, bottom) show excellent agreement with the experiment from 0° to 10.5°. We expect this to be the case only for mild AOAs before approaching stall conditions since our ASM does not capture the mechanisms of flow separation. Thus, through this swept-wing case, we gain confidence that our ASM yields accurate predictions in conditions with spanwise flow up to a moderate AOA.

# **B.** Isolated Propeller

In order to validate our propeller ALM, we simulated the Beaver propeller used in the experimental work by Veldhuis [52]. This four-bladed propeller is 0.237 m in diameter, and, even though its design is outdated, it has been thoroughly tested experimentally and computationally by the Flight Performance and Propulsion research group at Delft University of Technology, producing abundant data for model validation. The propeller was simulated across a range of advance ratio  $J = V_{\infty}/nD$ , with a diameter-based Reynolds number at 70% the blade span  $\text{Re}_D = \frac{0.7\pi nD^2}{v}$  of approximately  $1.8 \times 10^6$ , where n is the rotations per second. The geometry of the blade is reported in Sinnige et al. [54] No collective pitch was used, resulting in a blade pitch angle of 23.9° at the radial position r/R = 0.75. The propeller thrust, torque, and propulsive efficiently predicted with our meshless LES are compared in Fig. 10 to experimental and numerical results reported in the literature, showing satisfactory agreement across advance ratio.

Propellers often operate at a mild incidence angle. This is due to the pitch of the vehicle, turning of the flow by the wing, or both. In order to validate the accuracy of our simulations at an incidence angle, the Beaver propeller was simulated ranging its angle of attack relative to the freestream from  $0^{\circ}$  to  $20^{\circ}$ . Fig. 11 compares the predicted thrust to the experimental measurements reported by Sinnige et al. [56] as the incidence angle is increased at a variety of advance ratios, showing reasonable agreement with the experiment.

In order to validate the blade loading predicted by our ALM, we simulated the Beaver propeller at an advance ratio J of 0.8 at no incidence angle. Fig. 12 shows the thrust history of our meshless LES converging to a mean value of 0.0935, which is within 1.6% of the experimental mean  $C_T$  of 0.0953 reported by Sinnige et al. [54]. Fig. 12 also shows the mean  $C_T$  of a detached-eddy simulation (DES) reported by Chu et al. [57] and unsteady Reynolds-average Navier-Stokes (URANS) reported by Stokkermans et al. [20], which are respectively within 1.4% and 6.6% of the experimental measurement. Fig. 13 shows the sectional thrust and torque along the blade in our meshless LES predicted by the actuator line model, compared to the blade-resolved URANS simulation. Both approaches show good agreement away from the spinner. A slight discrepancy is observed towards the spinner in the region r/R < 0.35, which is likely caused by the mounting pod and the cylindrical section near the root. The mounting pod, which is included in the

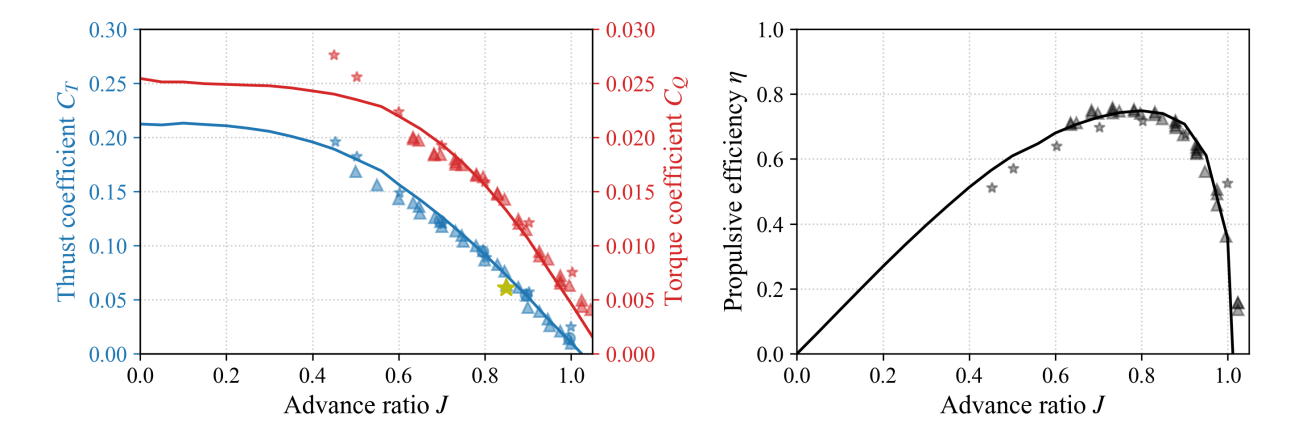


Fig. 10 Isolated Beaver propeller in forward flight. Simulations: - rVPM; ★ URANS by Sinnige et al. [55]. Experimental: △ Sinnige et al. [56]; ○ Sinnige et al. [54]; ★ Veldhuis [52].

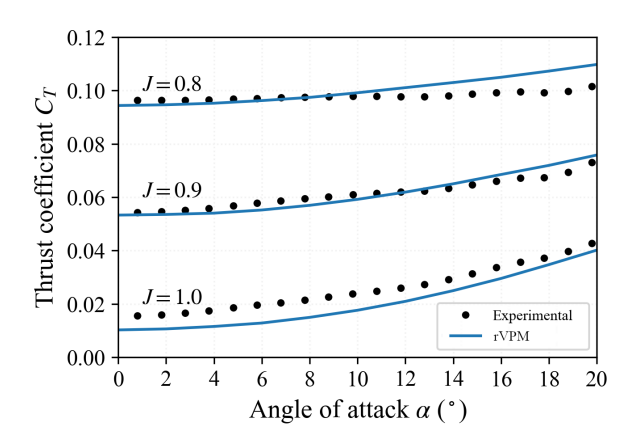


Fig. 11 Simulation of Beaver propeller at an incidence angle, compared to experimental measurements reported by Sinnige et al. [56].

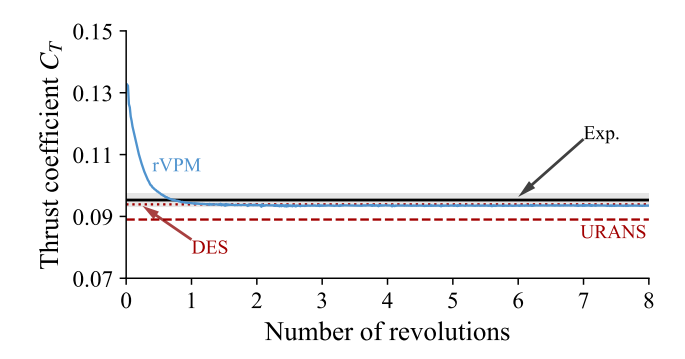


Fig. 12 Thrust history of Beaver propeller simulation using meshless LES (rVPM), compared to mean  $C_T$  of experiment [54], URANS [20], and DES [57]. Shaded region encompasses the 95%-confidence interval of the experiment.

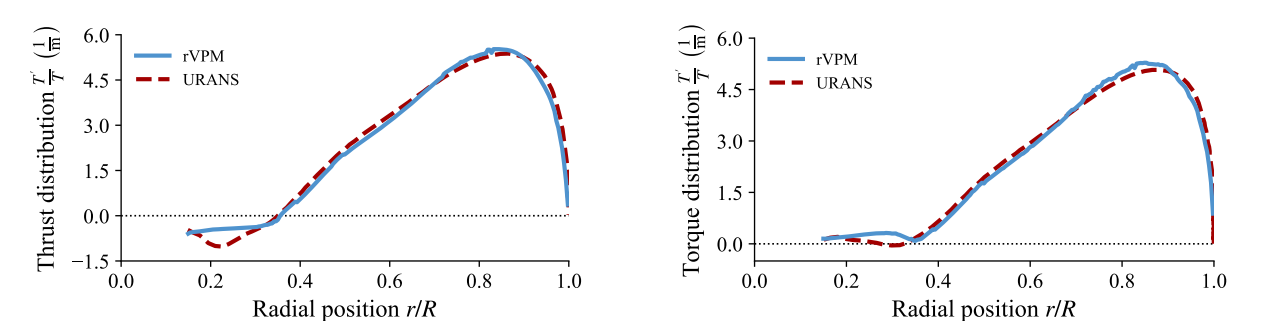


Fig. 13 Time-average thrust and power distribution of Beaver propeller in meshless LES (rVPM) with actuator line model, compared to blade-resolved URANS results reported by Stokkermans et al. [20]

URANS while ignored in the rVPM, blocks the flow from the centerline up to r/R = 0.3, while the cylindrical root section does not transition into a streamlined shape until about  $r/R \approx 0.35$ , leading to separated flow over this entire section. The good agreement over the rest of the blade (which is responsible for most of the propeller performance) and the good agreement with the experimental mean  $C_T$  confirm that our ALM and meshless LES accurately predicts the loading and performance of the propeller.

# C. Propeller Wake

In order to validate the propeller wake resolved by our meshless LES, we compared the flow field to experimental and numerical results reported in the literature. This validation built on a prior study by the authors [2], in which a detailed convergence study was performed. The Beaver propeller was operated at an advance ratio J of 0.8 and freestream velocity  $V_{\infty}$  of 40 m/s at no incidence angle. This corresponds to a tip Mach number of 0.46 and a diameter-based Reynolds number of  $1.8 \times 10^6$  at 70% the blade span.

The spatial resolution in the wake is controlled by the number of times that particles are shed off the blade in a revolution, or  $N_{\rm sheds}$ , which was set to  $360 \times 4$ . This led to a spatial resolution of  $\Delta x \approx 0.004R$  at the tip vortex. The temporal resolution is controlled by the number of time steps per revolution, or  $N_{\rm steps}$ , which was set to 72. This is equivalent to steps of 5°, which is a rather coarse temporal resolution, but the results presented here will show that this is sufficient to fully resolve the wake close to the propeller. The number of blade elements  $n_{\rm blade}$  was set to 200. The initial core overlap  $\lambda \equiv \frac{\Delta x}{\sigma} = \frac{2\pi R}{\sigma N_{\rm sheds}}$  was set to 2.125 at the tip. The spatial discretization is visualized in Fig. 14, using up to 9.5M particles after eight revolutions. The simulation was run for eight revolutions and averaged quantities were calculated over the last three.

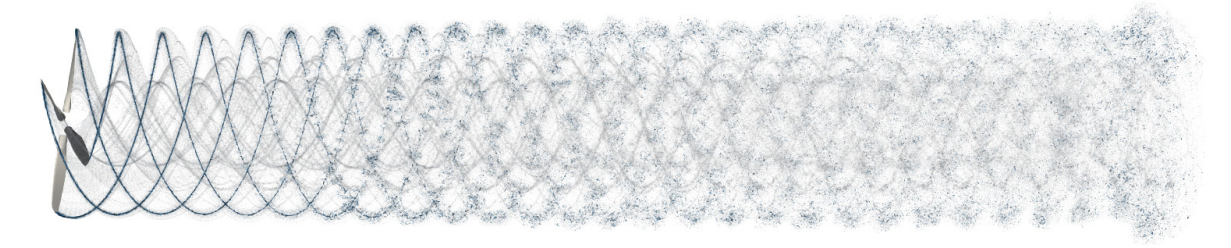


Fig. 14 Computational elements (vortex particles) in isolated Beaver propeller after 8 revolutions, resulting in 9.5 million particles. Vortex particles colored by strength.

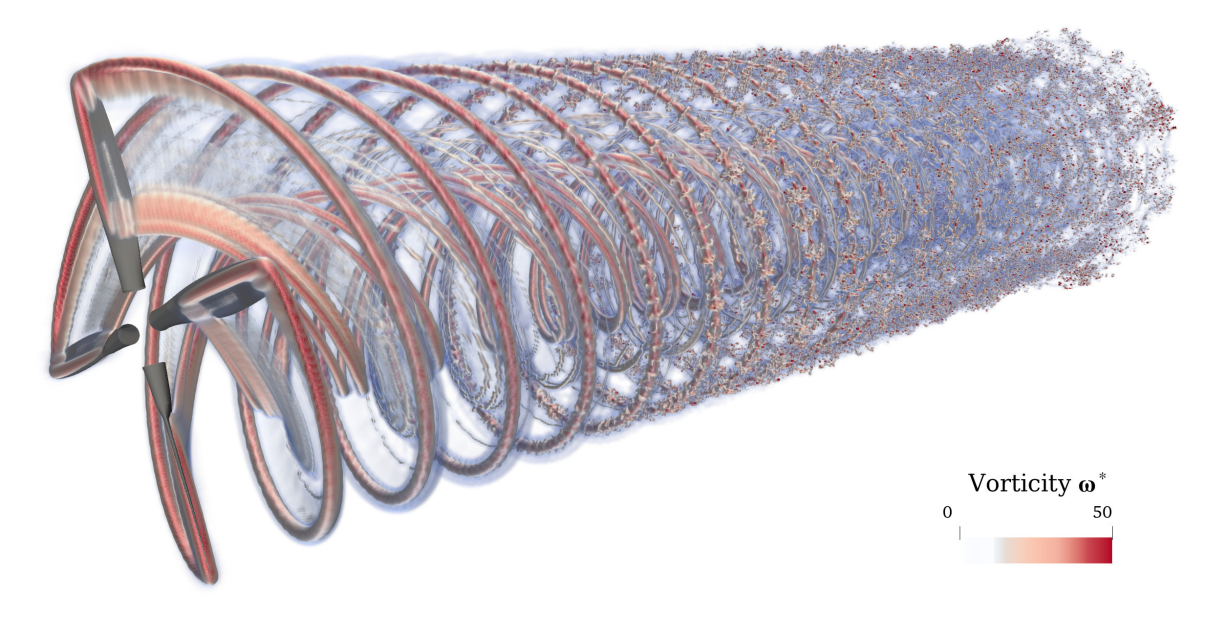


Fig. 15 Volume rendering of vorticity field in isolated Beaver propeller simulation.

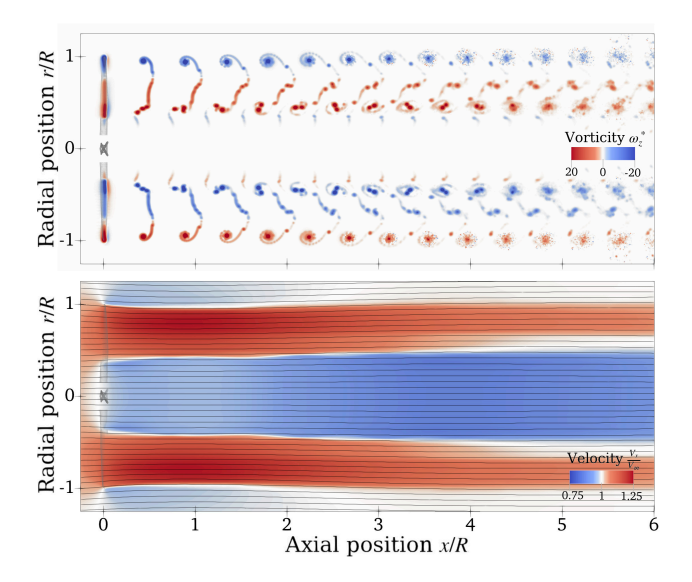


Fig. 16 Flow field in Beaver propeller simulation: (top) slice of ensemble-average in-plane vorticity and (bottom) time-average axial velocity and streamlines.

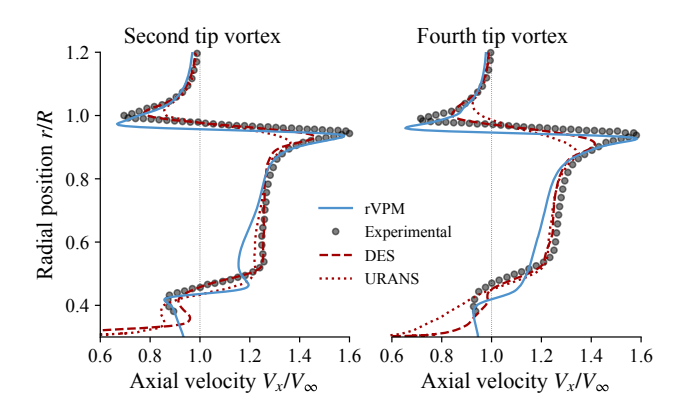


Fig. 17 Ensemble-average axial velocity probed across tip vortices as predicted by our meshless LES (rVPM), compared to mesh-based CFD simulations [20, 57] and experiment [54].

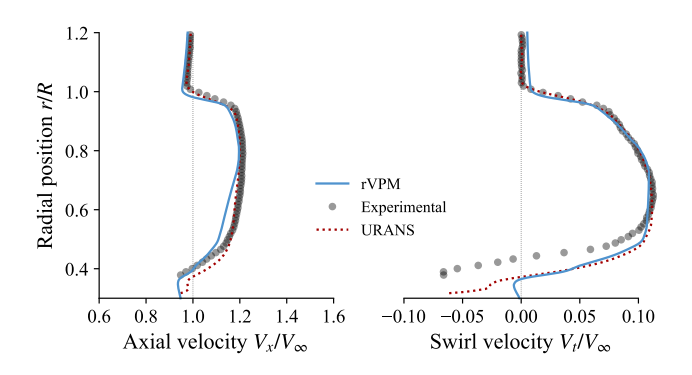


Fig. 18 Time-average velocity profile at r/R = 0.19 as predicted by our meshless LES, compared to URANS and experiment [58].

Fig. 15 visualizes the wake through a volume rendering of the vorticity field. In this and subsequent figures, the vorticity has been nondimensionalized as  $\omega^* \equiv \omega D/V_{\rm disk}$ , where D is the propeller diameter, and  $V_{\rm disk}$  is the equivalent actuator-disk velocity  $2V_{\rm disk} = V_{\infty} + \sqrt{V_{\infty}^2 + {}^8T/\rho\pi D^2}$ . The volume rendering shows the simulation capturing the fine vortical structure of the wake and the development of turbulence as the wake evolves. The wake structure is shown in Fig. 16 (top) through a slice of the ensemble-average in-plane vorticity taken as blades intersect the plane. In between the plane of rotation and x/R = 3, the inner vortex sheet stretches and folds around tip vortices. At x/R > 3, the inner sheet approaches the preceding tip vortex, causing it to deform and develop turbulence that eventually breaks the vortex down. The time-average axial velocity and streamlines are shown in Fig. 16 (bottom), where the streamtube is seen to contract between the plane of rotation and  $x/R \approx 1$ , after which it slowly expands as turbulence starts to develop.

Fig. 17 shows the axial velocity along the second and fourth tip vortices. The rVPM underpredicts the velocity in the inboard section r/R < 0.8 and tip vortices are slightly shifted inboard, both effects caused by omitting the flow blockage of the mounting pod. The rVPM, however, resolves the tip vortices with remarkable accuracy as evidenced by the velocity peaks near  $r/R \approx 1$ , outperforming both URANS and DES. As noted by Stokkermans et al. [20], the numerical dissipation associated with mesh-based CFD makes it computationally unfeasible to fully resolve the tip vortices. On the other hand, the low-numerical dissipation of our meshless LES makes it possible to preserve and resolve the vortical structure with minimal computational effort.

Fig. 18 shows the time-average velocity profile close to the plane of rotation as predicted by our meshless LES, compared to experimental and blade-resolved URANS results reported by van Arnhem [58]. Aside from the streamtube edge shifted inboard and the axial velocity slightly underpredicted for r/R < 0.8 (both effects caused by omitting the flow blockage of the mounting pod), Fig. 18 shows reasonable agreement between rVPM and both experiment and URANS.

All these results build our confidence that the propeller wake that will later be impinging on the wing is accurate and well resolved. Hence, any inconsistencies later encountered in the predicted propeller-wing interactions can be narrowed down to possible deficiencies of the wing's actuator surface model rather than the propeller wake.

# **IV. Propeller-Wing Interactions**

Having validated the wing and the propeller in isolation, we now place the wing in the wake of the propeller and incrementally validate each aspect of the interactions. First, wing and propeller are placed in a tip-mounted configuration. The wing has a low aspect ratio and a large flap, resembling a tailplane (or horizontal stabilizer) with tip-mounted propellers. At first, the system is simulated at zero angle of attack ( $\alpha=0^{\circ}$ ) at no elevator deflection ( $\delta_e=0^{\circ}$ ), hence, the aerodynamic wing load is caused purely by the swirl of the wake. The wing is then aerodynamically loaded by deflecting the elevator, which causes a mild turning of the propeller wake. Stronger turning of the propeller wake is tested by pitching the propeller-wing system to an AOA of  $10^{\circ}$ . All these cases are validated by comparison to experimental measurements reported in the literature. Finally, validation on a blown wing case is presented simulating the conventional configuration of a propeller mounted mid-span on a main wing at multiple AOAs.

# A. Tip-Mounted Propeller

We will now look at the interactions in a tip-mounted configuration, simulating the experiment performed by van Arnhem known as *PROWIM-HTP*, shown in Fig. 19. van Arnhem et al. [59] conducted the PROWIM-HTP study of propeller-wing interactions on a tip-mounted propeller configuration using the Beaver propeller, which was further expounded in van Arnhem's doctoral thesis [58]. This dataset was later used to validate a URANS study of propeller-wing interactions by Stokkermans et al. [20], further expounded in Stokkermans' doctoral thesis [60]. The configuration used a straight wing with low aspect ratio (b/c = 2.7), symmetric NACA 642-A015 profile, and a 25%-chord flap spanning 62% of the semi-span. This geometry resembles a tailplane (or horizontal stabilizer) with tip-mounted propellers.

The wing has a span b of 0.654 m, while the diameter D of the Beaver propeller is 0.237 m. Propeller and wing share the same angle of attack. Each test uses a freestream velocity  $V_{\infty}$  of 40 m/s, advance ratio J of 0.8, and inboard-up propeller rotation, unless otherwise indicated. This corresponds to a diameter-based Reynolds number of  $1.8 \times 10^6$  at 70% of the blade span and a tip Mach number of 0.46 for the prop, and a chord-based Reynolds number of  $0.7 \times 10^6$  for the wing. The flow over the wing was tripped close to the leading edge in the experiment. No collective pitch is used, which, as shown in Section III.C, leads to a thrust coefficient  $C_T = T/\rho n^2 D^4$  of 0.0935 in our simulations, while van Arnhem reported an experimental  $C_T$  of 0.0936. Our simulation is shown in Fig. 20, visualizing the wake structure in

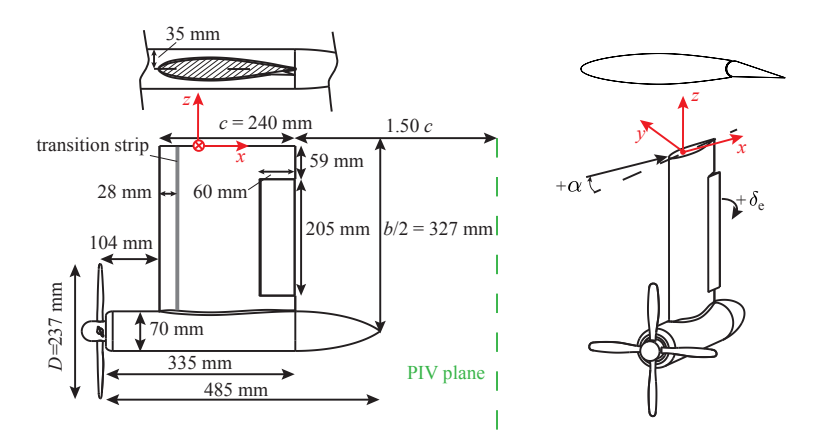


Fig. 19 Tailplane with tip-mounted propeller case, or PROWIM-HTP. Diagram reprinted from van Arnhem et al. [59] with permission from copyright holder.

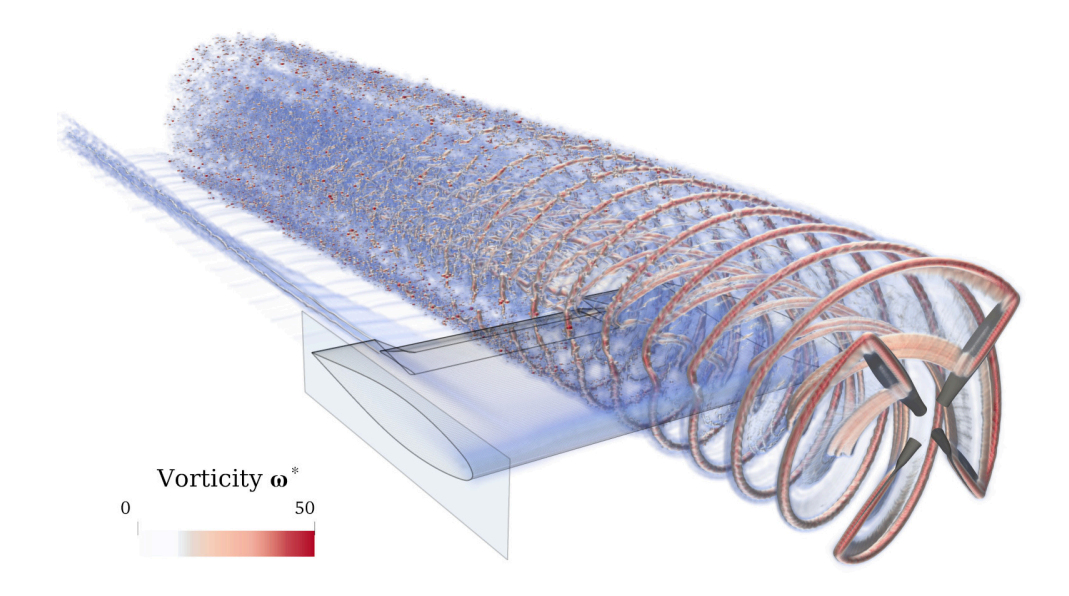


Fig. 20 Volume rendering of vorticity in simulation of tailplane with tip-mounted propeller. Case  $\alpha = 0^{\circ}$ ,  $\delta_e = +10^{\circ}$ , and J = 0.8.

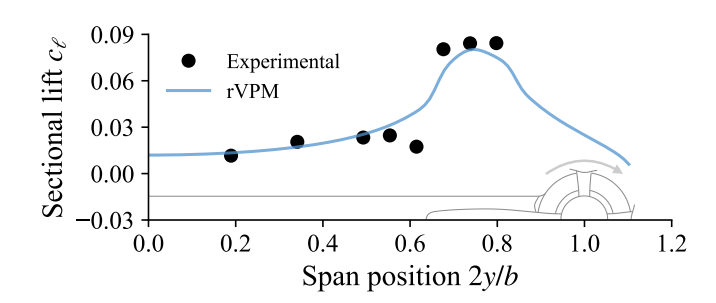


Fig. 21 Time-average load distribution in tip-mounted case with propeller blowing on flat wing ( $\alpha=0^{\circ}$ ,  $\delta_e=0^{\circ}$ , and inboard-up rotation direction).

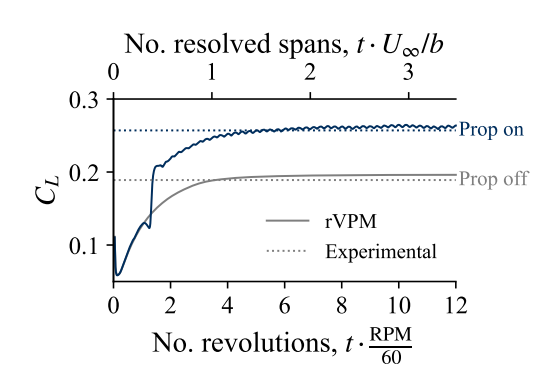


Fig. 22 History of  $C_L$  in tip-mounted case with and without propeller. Test at  $\alpha=0^\circ$ ,  $\delta_e=+10^\circ$ , and inboard-up rotation direction.

presence of the wing.

Propeller-wing interactions were introduced with incremental complexity. First, the prop-wing system was tested at zero angle of attack ( $\alpha = 0^{\circ}$ ) and no elevator deflection ( $\delta_e = 0^{\circ}$ ), with the wing simply acting as a flat plate. Hence, the aerodynamic wing load was caused purely by the swirl of the wake. The predicted wing loading is shown in Fig. 21, showing reasonable agreement with the experiment. Since this load is caused entirely by the wake swirl, these favorable results give us confidence that both the circulation solver and force calculation in the ASM are physically accurate beyond the simple case of a uniform freestream.

Next, the wing was aerodynamically loaded by deflecting the elevator by  $\delta_e = +10^\circ$ . Fig. 22 shows the history of the lift generated by the wing with and without the propeller running. In both cases,  $C_L$  seems to converge after about seven rotor revolutions, equivalent to resolving the wake for about two span-distances. Hence, all simulation were run for 12 revolutions and all results will hereon be reported considering only the last four revolutions.

When the wing generates lift through elevator deflection, the elevator also causes a mild turning of the rpropeller wake, which enhances the circulation and lift of the wing. On the case  $\alpha=0^\circ$  and  $\delta_e=+10^\circ$ , Stokkermans reported an experimental mean  $C_L$  that increases from 0.189 when the prop is off to 0.257 when the prop is on, leading to a lift augmentation of 36% due to beneficial prop-on-wing interactions. As shown in Fig. 22, our simulation converges to a mean  $C_L$  of 0.196 and 0.262 when the prop is off and on, respectively, leading to a lift augmentation of 34%. In order to confirm that our predicted lift augmentation is caused by the correct physical mechanisms, Fig. 23 shows the vorticity at a plane downstream of the wing compared to experimental particle image velocimetry (PIV) reported by van Arnhem. The vortices shed by the inboard and outboard elevator edges are seen at  $2y/b \approx 0.2$  and  $2y/b \approx 0.8$ , respectively, along with the tip vortex at  $2y/b \approx 1$ . The propeller slipstream surrounds the tip vortex and is deformed by the wing surface in qualitative agreement with the experiment. Fig. 24 shows slices of the vorticity across the elevator vortex and tip vortex encompassed by the slipstream, evidencing quantitative agreement between simulation and experiment. This good agreement between the flow field predicted by our meshless LES and the experiment shows that the interactions between the propeller wake and the wing surface captured by our ASM, which lead to lift augmentation, are physically correct.

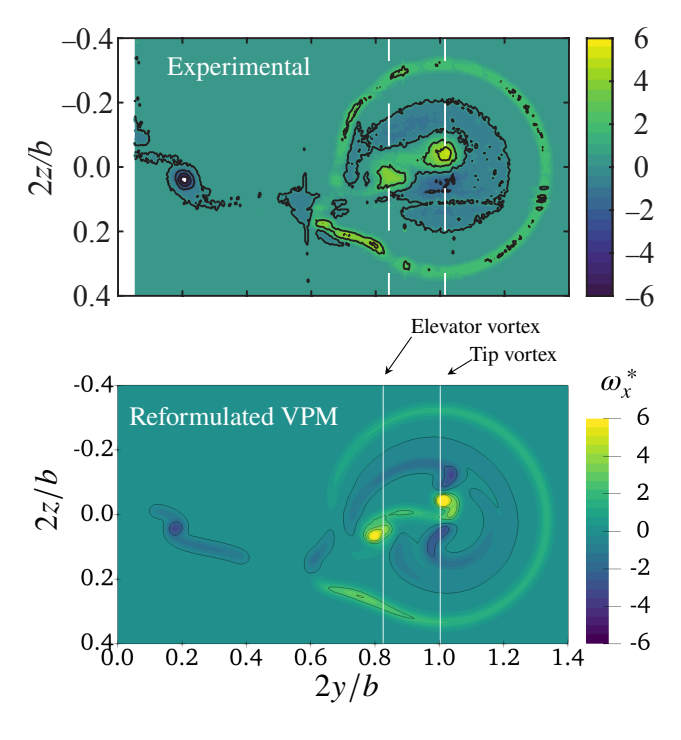


Fig. 23 Time-average axial vorticity in tip-mounted case at plane 1.5c from trailing edge, (top) measured experimentally and (bottom) predicted with our meshless LES. Case  $\alpha = 0^{\circ}$ ,  $\delta_e = +10^{\circ}$ , and J = 0.8. Experimental PIV (top) reprinted from van Arnhem's doctoral thesis [58] with permission from copyright holder.

 $<sup>\</sup>P$ Since our ASM assumes wing elements with a straight chord, the elevator deflection is modeled as an equivalent twist of the elements about the quarter-chord line, varying from  $3.75^{\circ}$  inboard to  $6.5^{\circ}$  outboard of the elevator section. This equivalent twist was determined matching the experimental wing loading in the prop-off case.

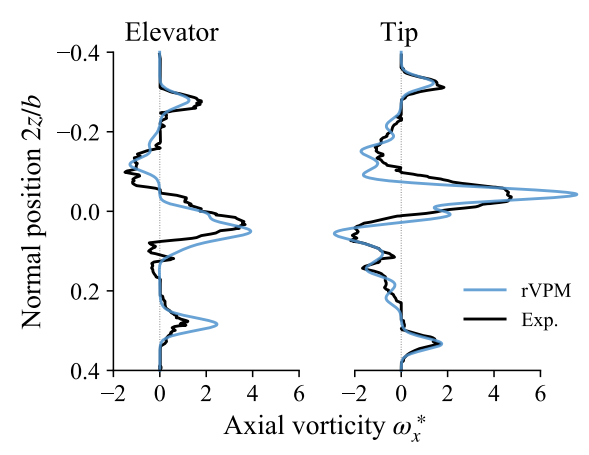


Fig. 24 Time-average vorticity across elevator and tip vortices shown in Fig. 23.

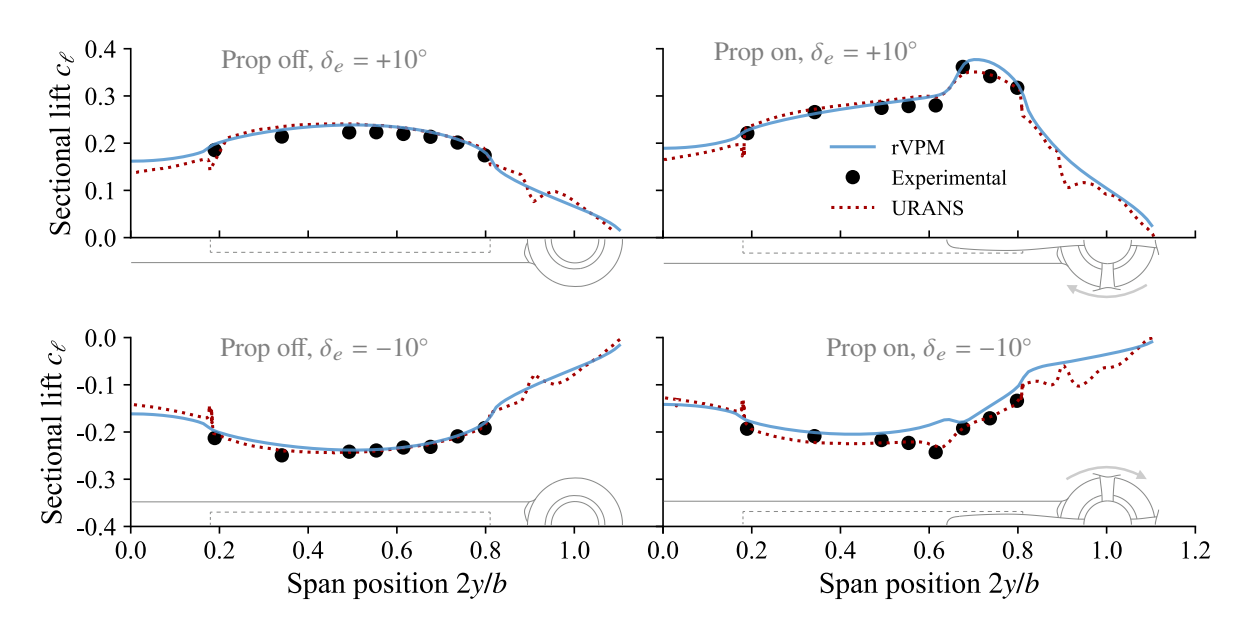


Fig. 25 Time-average lift distribution in tip-mounted case with positive and negative elevator deflection  $\delta_e$  at  $\alpha=0^\circ$ , compared to URANS an experiment by van Arnhem et al. [59]. Inboard-up rotation direction.

The lift distribution with propeller on and off is shown in Fig. 25, and compared to the experiment with both positive and negative elevator deflection ( $\delta_e = \pm 10^\circ$  and  $\alpha = 0^\circ$ ). As a reference, Fig. 25 also includes the lift distribution reported by van Arnhem et al. [59] with URANS. The URANS simulation fully resolves the wing surface down to a  $y^+$  of 1 in the boundary layer, in contrast to our LES that simply models the wing through an actuator surface model. When  $\delta_e$  is positive, Fig. 25 (top) shows good agreement between our meshless LES and both the experiment and URANS. When  $\delta_e$  is negative, Fig. 25 (bottom) shows some discrepancies, but overall the loading is in within reasonable agreement. This shows that the ASM is able to accurately predict the wing loading with minimal computational effort. Our predictions were also tested at different thrust settings by varying the advance ratio J. Fig. 26 shows that good agreement between our LES and the experiment is maintained as the propeller thrust increases.

Finally, stronger propeller-wing interactions were tested by pitching the wing system to an angle of attack of 10°. In this setting, the circulation of the wing becomes strong, more prominently turning the propeller slipstream. Also, since the angle of attack sets the propeller at an incidence angle relative to the freestream, the freestream pushes the wake against the wing's lower surface while also creating an asymmetric slipstream with advancing and retreating sides. Fig. 27 shows the wing loading, finding good agreement between simulation and experiment.

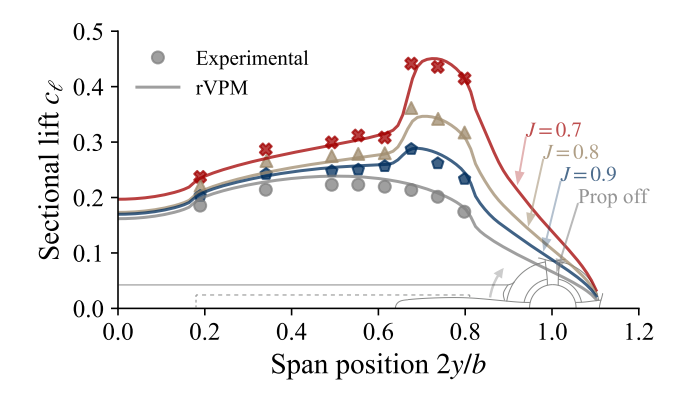


Fig. 26 Time-average lift distribution in tip-mounted case as propeller thrust is increased. Test at  $\alpha = 0^{\circ}$ ,  $\delta_e = +10^{\circ}$ , and inboard-up rotation direction.

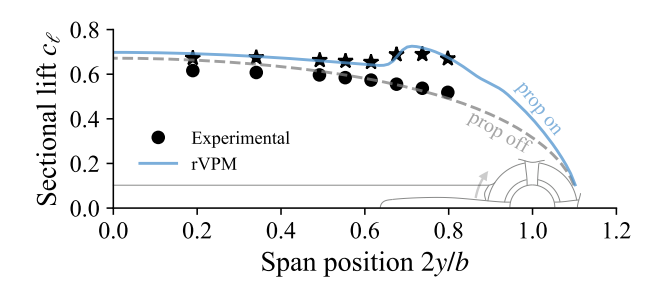


Fig. 27 Time-average lift distribution in tip-mounted case at angle of attack  $\alpha=10^{\circ}$ . Test with  $\delta_e=0^{\circ}$  and inboard-up rotation direction.

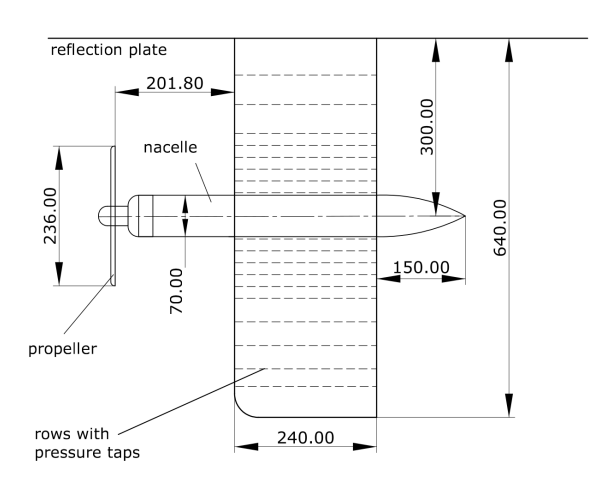


Fig. 28 Description of blown-wing case, or PROWIM, with propeller mounted mid-span. Dimensions in mm. Diagram reprinted from Veldhuis' doctoral thesis [52].

# **B. Blown-Wing Case**

We will now look at the interactions in a conventional configuration where the propeller is mounted mid-span. In this configuration, the full slipstream interacts with the wing (as opposed to the tip-mounted case where only the inboard part of the slipstream does); hence, this case is referred to as the "blown wing" case. For this case, we simulated the experiment performed by Veldhuis [52] known as *PROWIM*, shown in Fig. 28.

The configuration uses a straight wing with aspect ratio b/c = 5.33, symmetric NACA 642-A015 profile, a span b of

1.28 m, and the Beaver propeller mounted at the span position 2y/b = 0.469. Propeller and wing share the same angle of attack. Each test uses a freestream velocity  $V_{\infty}$  of 49.5 m/s and an advance ratio J of 0.85. This leads to similar Reynolds and Mach numbers as in the tip-mounted case. The experiment was reportedly conducted at a thrust setting  $T_c = T/\rho V_{\infty}^2 D^2$  of 0.168 (corresponding to a thrust coefficient  $C_T = T/\rho n^2 D^4$  of 0.121). A collective pitch of 2° was used in the simulation in order to match that thrust setting, leading to a blade angle of 25.9° at the radial position r/R = 0.75. The simulation then resulted in  $T_c = 0.160$  (or  $C_T = 0.117$ ), which is a thrust 5% lower than used in the experiment, but we deemed this difference to be negligible.

The blown wing was tested as the angle of attack varied from  $0^{\circ}$  to  $10^{\circ}$ , while determining the effects of propeller rotation direction. Fig. 29 shows the distribution of force normal to the wing, as predicted with our simulation and compared to the experiment. The cases with  $\alpha=0^{\circ}$  (where the wing acts as a flat plate) and  $\alpha=4^{\circ}$  (where the wing turns the slipstream) agree reasonably well with the experiment, showing the loading increasing where the blade goes up, while decreasing where the blade goes down. These changes in the loading are caused by the swirl direction locally increasing or decreasing the AOA of the wing. In the case with  $\alpha=10^{\circ}$ , these dynamics change due to the stronger nature of the interactions. For instance, notice in both simulation and experiment that the loading no longer drops where the blade goes down. This is because the effects of turning the slipstream become stronger than the effects of swirl. Even though the simulation shows the right trend, it overpredicts the lift augmentation in the slipstream at this AOA. Noticing that the prop off case also overpredicts the loading, it is possible that the wing in the experiment is mildly stalled at  $\alpha=10^{\circ}$ . This could drive the discrepancy between simulation and experiment since our ASM does not capture stalled conditions. In light of this, we conclude that our LES simulation accurately predicts propeller-wing interactions

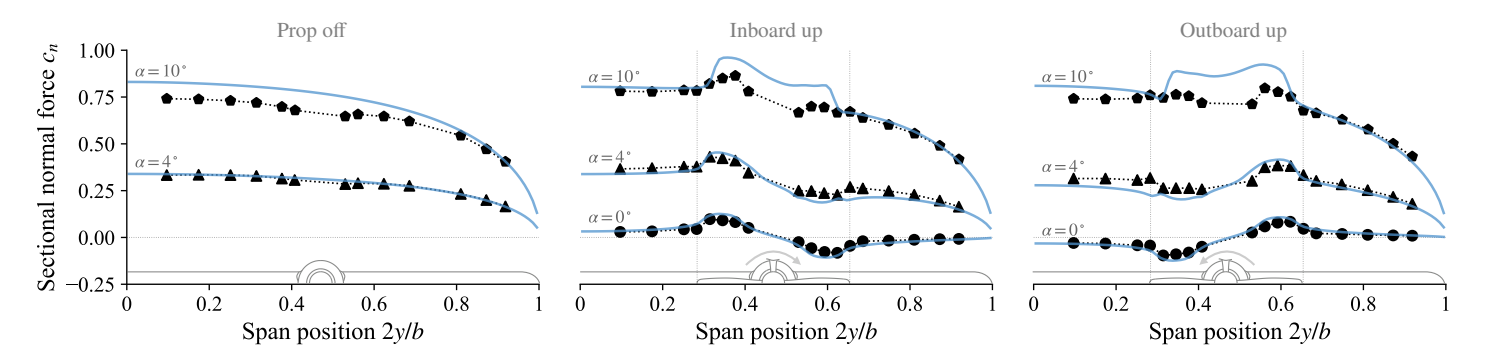


Fig. 29 Time-average normal force distribution in blown-wing case at multiple angles of attack  $\alpha$  (left) without the propeller, (middle) with the propeller rotating inboard up, and (right) outboard up. rVPM simulation (solid lines) compared to experimental measurements (markers) reported by Veldhuis [52].

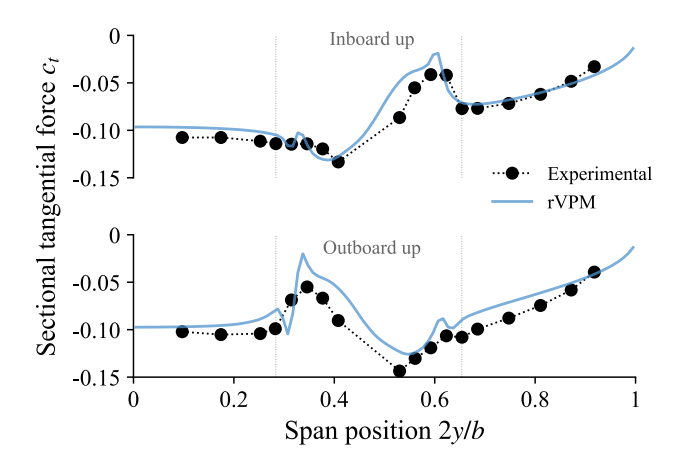


Fig. 30 Time-average tangential force in blown-wing case at angle of attack  $\alpha = 10^{\circ}$ .

up to a moderate angle of attack.

In the previous tests we have discussed only the interactional effects on normal force or lift, however, the drag force is also accurately captured. To show this, Fig. 30 compares our simulation to the tangential force reported by Veldhuis at  $\alpha=10^\circ$ . This tangential force was measured experimentally integrating pressure taps around the wing profile, hence it includes form and induced drag, while excluding skin friction drag. Since this force is tangential to the wing (and not to the freestream), it also includes a small component of lift. In both rotation directions, the simulation agrees reasonably well with the experiment, giving confidence that the drag is accurately predicted.

# V. Conclusion

In this study, we have presented a CFD framework based on the reformulated VPM for simulating complex propeller-wing aerodynamic interactions. Building on a meshless LES scheme that is one to two orders of magnitude faster than conventional mesh-based CFD, we included propellers and wings in the computational domain through actuator models. Propeller blades were captured through an actuator line model, which is a well-established practice for LES. A novel, vorticity-based, actuator surface model (ASM) was developed for wings, which is suitable for propeller-wing interactions when a wake impinges on the surface of a wing. This ASM imposes the no-flow-through condition at the airfoil centerline by calculating the circulation that meets this condition and by immersing the associated vorticity in the LES following a pressure-like distribution.

The interactions of a propeller wake impinging on a wing were validated comparing our meshless LES to experimental studies in the literature. First, wing and propeller were simulated in isolation, finding that our meshless LES is able to resolve the structure of the propeller wake with remarkable accuracy and little computational resources. Next, the wing was placed in the wake of the propeller in a tip-mounted configuration. The case with the wing acting as a flat plate showed that the ASM accurately calculates the loading on the wing caused by the propeller swirl. The case with elevator deflection showed that our meshless LES captures the physical mechanisms that lead to lift augmentation when the wing surface deflects the propeller slipstream. Stronger propeller-wing interactions were tested by pitching the wing system to an angle of attack of 10°, finding good agreement between simulation and experiment. Finally, a blown-wing configuration was tested at multiple angles of attack and different rotation directions, showing our simulations to be accurate up to AOAs approaching stall.

Previous studies [20, 57] have shown that mesh-based URANS and DES do as well at predicting propeller-wing interactions as the meshless LES method presented here. However, we highlight that our proposed approach achieves the same level of accuracy without the hurdles of generating a mesh and with much lower computational cost. In fact, each simulation in this study was ran in a single computing EPYC 7702 node within a matter of hours or day.

This study validates our meshless LES as an accurate approach for predicting complex interactional aerodynamics. We have focused on the high fidelity achieved with rVPM; however, since this CFD is not limited by the classic CFL condition, rVPM can be used across all levels of fidelity, all in the same framework by simply coarsening or refining the simulation. In the low end of fidelity, simulations are similar to a free-wake method, while in the high end simulations become meshless large eddy simulations. Thus, rVPM can be used by aircraft designers as a high-fidelity tool that is one to two orders of magnitude faster than conventional mesh-based CFD, or as a variable-fidelity tool for the different stages of design.

# **Acknowledgments**

This material is based upon work supported by National Science Foundation under Grant No. 2006219. Any opinions, findings, and conclusions or recommendations expressed in this material are those of the author(s) and do not necessarily reflect the views of the National Science Foundation.

The simulations presented in this study used the open-source framework FLOWUnsteady [29], which uses the open-source code FLOWVPM [2] developed by the authors and a modified version of the open-source code ExaFMM [48] originally developed by Lorena Barba and Rio Yokota. FLOWUnsteady is implemented in the Julia programming language [49] and integrates the open-source software ParaView [61, 62] as its visualization engine.

# References

[1] Winckelmans, G., and Leonard, A., "Contributions to Vortex Particle Methods for the Computation of Three-Dimensional Incompressible Unsteady Flows," *Journal of Computational Physics*, Vol. 109, No. 2, 1993, pp. 247–273. https://doi.org/10.1006/jcph.1993.1216, URL http://linkinghub.elsevier.com/retrieve/pii/S0021999183712167.

- [2] Alvarez, E. J., and Ning, A., "A Stable Vortex Particle Method Formulation for Meshless Large Eddy Simulation," *AIAA Journal (accepted)*, 2023. URL https://arxiv.org/abs/2206.03658.
- [3] Alvarez, E. J., and Ning, A., "Development of a Vortex Particle Code for the Modeling of Wake Interaction in Distributed Propulsion," 2018 Applied Aerodynamics Conference, American Institute of Aeronautics and Astronautics, 2018, pp. 1–22. https://doi.org/10.2514/6.2018-3646, URL https://arc.aiaa.org/doi/10.2514/6.2018-3646.
- [4] Alvarez, E. J., and Ning, A., "Modeling Multirotor Aerodynamic Interactions Through the Vortex Particle Method," *AIAA Aviation 2019 Forum*, American Institute of Aeronautics and Astronautics, Dallas, Texas, 2019. https://doi.org/10.2514/6.2019-2827, URL https://arc.aiaa.org/doi/10.2514/6.2019-2827.
- [5] Alvarez, E. J., Schenk, A., Critchfield, T., and Ning, A., "Rotor-on-Rotor Aeroacoustic Interactions of Multirotor in Hover," *The Vertical Flight Society's 76th Annual Forum*, 2020. URL https://scholarsarchive.byu.edu/facpub/4053/.
- [6] Lee, H., and Lee, D. J., "Rotor interactional effects on aerodynamic and noise characteristics of a small multirotor unmanned aerial vehicle," *Physics of Fluids*, Vol. 32, No. 4, 2020. https://doi.org/10.1063/5.0003992, URL https://doi.org/10.1063/5.0003992.
- [7] Zanotti, A., and Algarotti, D., "Aerodynamic interaction between tandem overlapping propellers in eVTOL airplane mode flight condition," *Aerospace Science and Technology*, Vol. 124, 2022, p. 107518. https://doi.org/10.1016/j.ast.2022.107518.
- [8] Arda Yücekayali, "Noise Minimal & Green Trajectory And Flight Profile Optimization For Helicopters," Ph.D. thesis, Middle East Technical University, 2020.
- [9] Jacobellis, G., Singh, R., Johnson, C., Sirohi, J., and McDonald, R., "Experimental and computational investigation of stacked rotor performance in hover," *Aerospace Science and Technology*, Vol. 1, 2021, p. 106847. https://doi.org/10.1016/j.ast.2021. 106847.
- [10] Zanotti, A., Savino, A., Palazzi, M., Tugnoli, M., and Muscarello, V., "Assessment of a Mid-Fidelity Numerical Approach for the Investigation of Tiltrotor Aerodynamics," *Applied Sciences*, Vol. 11, No. 8, 2021, p. 3385. https://doi.org/10.3390/app11083385, URL https://www.mdpi.com/2076-3417/11/8/3385.
- [11] Tugnoli, M., Montagnani, D., Syal, M., Droandi, G., and Zanotti, A., "Mid-fidelity approach to aerodynamic simulations of unconventional VTOL aircraft configurations," *Aerospace Science and Technology*, Vol. 115, 2021, p. 106804. https://doi.org/10.1016/j.ast.2021.106804.
- [12] Alvarez, E. J., "Reformulated Vortex Particle Method and Meshless Large Eddy Simulation of Multirotor Aircraft," Ph.D. thesis, Brigham Young University, 2022. URL https://scholarsarchive.byu.edu/etd/9589.
- [13] Angot, P., Bruneau, C.-H., and Fabrie, P., "A penalization method to take into account obstacles in incompressible viscous flows," *Numerische Mathematik*, Vol. 81, No. 4, 1999, pp. 497–520. https://doi.org/10.1007/s002110050401, URL http://link.springer.com/10.1007/s002110050401.
- [14] Sanderse, B., Pijl, S., and Koren, B., "Review of computational fluid dynamics for wind turbine wake aerodynamics," *Wind Energy*, Vol. 14, No. 7, 2011, pp. 799–819. https://doi.org/10.1002/we.458, URL http://oai.cwi.nl/oai/asset/17492/17492A.pdfhttps://onlinelibrary.wiley.com/doi/10.1002/we.458.
- [15] Fejtek, I., and Roberts, L., "Navier-Stokes computation of wing/rotor interaction for a tilt rotor in hover," *AIAA Journal*, Vol. 30, No. 11, 1992, pp. 2595–2603. https://doi.org/10.2514/3.11272, URL https://arc.aiaa.org/doi/10.2514/3.11272.
- [16] Rajagopalan, R. G., and Mathur, S. R., "Three Dimensional Analysis of a Rotor in Forward Flight," *Journal of the American Helicopter Society*, Vol. 38, No. 3, 1993, pp. 14–25. https://doi.org/10.4050/JAHS.38.14, URL https://www.ingentaconnect.com/content/10.4050/JAHS.38.14.
- [17] Sorensen, J. N., and Shen, W. Z., "Numerical Modeling of Wind Turbine Wakes," *Journal of Fluids Engineering*, Vol. 124, No. 2, 2002, pp. 393–399. https://doi.org/10.1115/1.1471361, URL https://asmedigitalcollection.asme.org/fluidsengineering/article/124/2/393/444521/Numerical-Modeling-of-Wind-Turbine-Wakes.
- [18] Churchfield, M. J., Schreck, S. J., Martinez, L. A., Meneveau, C., and Spalart, P. R., "An Advanced Actuator Line Method for Wind Energy Applications and Beyond," 35th Wind Energy Symposium, American Institute of Aeronautics and Astronautics, Reston, Virginia, 2017. https://doi.org/10.2514/6.2017-1998, URL https://arc.aiaa.org/doi/10.2514/6.2017-1998.
- [19] Troldborg, N., Zahle, F., Réthoré, P.-E., and Sorensen, N., "Comparison of the wake of different types of wind turbine CFD models," 50th AIAA Aerospace Sciences Meeting including the New Horizons Forum and Aerospace Exposition, American Institute of Aeronautics and Astronautics, Reston, Virigina, 2012. https://doi.org/10.2514/6.2012-237, URL https://arc.aiaa.org/doi/10.2514/6.2012-237.

- [20] Stokkermans, T. C. A., van Arnhem, N., Sinnige, T., and Veldhuis, L. L. M., "Validation and Comparison of RANS Propeller Modeling Methods for Tip-Mounted Applications," *AIAA Journal*, Vol. 57, No. 2, 2019, pp. 566–580. https://doi.org/10.2514/1.J057398, URL https://arc.aiaa.org/doi/10.2514/1.J057398.
- [21] Shen, W. Z., Zhang, J. H., and Sørensen, J. N., "The Actuator Surface Model: A New Navier-Stokes Based Model for Rotor Computations," *Journal of Solar Energy Engineering*, Vol. 131, No. 1, 2009, pp. 0110021–0110029. https://doi.org/10.1115/1.3027502, URL https://asmedigitalcollection.asme.org/solarenergyengineering/article/doi/10.1115/1.3027502/444133/The-Actuator-Surface-Model-A-New-NavierStokes.
- [22] Dobrev, I., Massouh, F., and Rapin, M., "Actuator surface hybrid model," *Journal of Physics: Conference Series*, Vol. 75, No. 1, 2007, p. 012019. https://doi.org/10.1088/1742-6596/75/1/012019, URL https://iopscience.iop.org/article/10.1088/1742-6596/75/1/012019.
- [23] Linton, D., Barakos, G., Widjaja, R., and Thornber, B., "Coupling of an Unsteady Aerodynamics Model with a Computational Fluid Dynamics Solver," *AIAA Journal*, Vol. 56, No. 8, 2018, pp. 3153–3166. https://doi.org/10.2514/1.J056784, URL https://arc.aiaa.org/doi/10.2514/1.J056784.
- [24] Chatelain, P., Backaert, S., Winckelmans, G., and Kern, S., "Large eddy simulation of wind turbine wakes," Flow, Turbulence and Combustion, Vol. 91, No. 3, 2013, pp. 587–605. https://doi.org/10.1007/s10494-013-9474-8.
- [25] Backaert, S., Chatelain, P., and Winckelmans, G., "Vortex Particle-Mesh with Immersed Lifting Lines for Aerospace and Wind Engineering," *Procedia IUTAM*, Vol. 18, 2015, pp. 1–7. https://doi.org/10.1016/j.piutam.2015.11.001, URL http://dx.doi.org/10.1016/j.piutam.2015.11.001.
- [26] Chatelain, P., Duponcheel, M., Caprace, D.-G., Marichal, Y., and Winckelmans, G., "Vortex particle-mesh simulations of vertical axis wind turbine flows: from the airfoil performance to the very far wake," Wind Energy Science, Vol. 2, No. 1, 2017, pp. 317–328. https://doi.org/10.5194/wes-2-317-2017, URL http://stacks.iop.org/1742-6596/753/i=3/a=032007?key=crossref.fc2b2fe9996c69d4a419caec4e075875https://www.wind-energ-sci.net/2/317/2017/.
- [27] Caprace, D.-G., Winckelmans, G., and Chatelain, P., "An immersed lifting and dragging line model for the vortex particle-mesh method," *Theoretical and Computational Fluid Dynamics*, No. iMMC, 2020. https://doi.org/10.1007/s00162-019-00510-1, URL https://doi.org/10.1007/s00162-019-00510-1http://link.springer.com/10.1007/s00162-019-00510-1.
- [28] Caprace, D.-G., Chatelain, P., and Winckelmans, G., "Wakes of rotorcraft in advancing flight: A large-eddy simulation study," *Physics of Fluids*, Vol. 32, No. 8, 2020, p. 087107. https://doi.org/10.1063/5.0015162, URL https://doi.org/10.1063/5.0015162http://aip.scitation.org/doi/10.1063/5.0015162.
- [29] Alvarez, E. J., and Ning, A., "FLOWUnsteady: An Interactional Aerodynamics Solver for Multirotor Aircraft and Wind Energy," *AIAA AVIATION 2022 Forum*, Chicago, IL, 2022. https://doi.org/10.2514/6.2022-3218.
- [30] Shankar, S., and Dommelen, L., "A New Diffusion Procedure for Vortex Methods," *Journal of Computational Physics*, Vol. 127, No. 1, 1996, pp. 88–109. https://doi.org/10.1006/jcph.1996.0160, URL https://linkinghub.elsevier.com/retrieve/pii/ S0021999196901606.
- [31] Gharakhani, A., "Grid-free simulation of 3-D vorticity diffusion by a high-order vorticity redistribution method," 15th AIAA Computational Fluid Dynamics Conference, No. June 2001, 2001. https://doi.org/doi:10.2514/6.2001-2640, URL http://dx.doi.org/10.2514/6.2001-2640.
- [32] Degond, P., and Mas-Gallic, S., "The Weighted Particle Method for Convection-Diffusion Equations. Part 1: The Case of an Isotropic Viscosity," *Mathematics of Computation*, Vol. 53, No. 188, 1989, p. 485. https://doi.org/10.2307/2008716, URL http://www.jstor.org/stable/2008717?origin=crossrefhttp://www.jstor.org/stable/2008716?origin=crossref.
- [33] Rossi, L. F., "Resurrecting Core Spreading Vortex Methods: A New Scheme that is Both Deterministic and Convergent," SIAM Journal on Scientific Computing, Vol. 17, No. 2, 1996, pp. 370–397. https://doi.org/10.1137/S1064827593254397, URL http://epubs.siam.org/doi/10.1137/S1064827593254397.
- [34] Winckelmans, G. S., "Some progress in large-eddy simulation using the 3D vortex particle method," *CTR Annual Research Briefs*, No. 2, 1995, pp. 391–415.
- [35] Mansfield, J. R., Knio, O. M., and Meneveau, C., "A Dynamic LES Scheme for the Vorticity Transport Equation: Formulation and a Priori Tests," *Journal of Computational Physics*, Vol. 145, No. 2, 1998, pp. 693–730. https://doi.org/10.1006/jcph.1998.6051.

- [36] Meneveau, C., Lund, T. S., and Cabot, W. H., "A Lagrangian dynamic subgrid-scale model of turbulence," *Journal of Fluid Mechanics*, Vol. 319, No. -1, 1996, p. 353. https://doi.org/10.1017/S0022112096007379, URL http://www.journals.cambridge.org/abstract{\_}S0022112096007379.
- [37] Winckelmans, G. S. S., "Topics in vortex methods for the computation of three and two dimensional incompressible unsteady flows," Phd thesis, California Institute of Technology, 1989. URL http://core.kmi.open.ac.uk/download/pdf/11813390.pdf.
- [38] Pedrizzetti, G., "Insight into singular vortex flows," *Fluid Dynamics Research*, Vol. 10, No. 2, 1992, pp. 101–115. https://doi.org/10.1016/0169-5983(92)90011-K.
- [39] Williamson, J. H., "Low-storage Runge-Kutta schemes," *Journal of Computational Physics*, Vol. 35, No. 1, 1980, pp. 48–56. https://doi.org/10.1016/0021-9991(80)90033-9.
- [40] Leonard, A., "Vortex methods for flow simulation," *Journal of Computational Physics*, Vol. 37, No. 3, 1980, pp. 289–335. https://doi.org/10.1016/0021-9991(80)90040-6, URL https://linkinghub.elsevier.com/retrieve/pii/0021999180900406.
- [41] Barba, L. A., Leonard, A., and Allen, C. B., "Advances in viscous vortex methods Meshless spatial adaption based on radial basis function interpolation," *International Journal for Numerical Methods in Fluids*, Vol. 47, No. 5, 2005, pp. 387–421. https://doi.org/10.1002/fld.811.
- [42] Barba, L. A., "Vortex Method for computing high-Reynolds number Flows: Increased accuracy with a fully mesh-less formulation," *California Institute of Technology*, Vol. 2004, 2004.
- [43] Torres, C. E., and Barba, L. A., "Fast radial basis function interpolation with Gaussians by localization and iteration," *Journal of Computational Physics*, Vol. 228, No. 14, 2009, pp. 4976–4999. https://doi.org/10.1016/j.jcp.2009.03.007, URL http://dx.doi.org/10.1016/j.jcp.2009.03.007.
- [44] Greengard, L. F., "The Rapid Evaluation Of Potential Fields In Particle Systems," Phd thesis, Yale University, 1987.
- [45] Cheng, H., Greengard, L., and Rokhlin, V., "A Fast Adaptive Multipole Algorithm in Three Dimensions," *Journal of Computational Physics*, Vol. 155, No. 2, 1999, pp. 468–498. https://doi.org/10.1006/jcph.1999.6355, URL http://www.sciencedirect.com/science/article/pii/S0021999199963556 [%] 5Cnhttp://linkinghub.elsevier.com/retrieve/pii/S0021999199963556.
- [46] Alvarez, E. J., and Ning, A., "High-Fidelity Modeling of Multirotor Aerodynamic Interactions for Aircraft Design," *AIAA Journal*, Vol. 58, No. 10, 2020, pp. 4385–4400. https://doi.org/10.2514/1.J059178, URL https://arc.aiaa.org/doi/10.2514/1.J059178.
- [47] Yokota, R., and Barba, L. A., "Treecode and fast multipole method for N-body simulation with CUDA," *GPU Computing Gems Emerald Edition*, 2011, pp. 113–132. https://doi.org/10.1016/B978-0-12-384988-5.00009-7.
- [48] Wang, T., Yokota, R., and Barba, L., "ExaFMM: a high-performance fast multipole method library with C++ and Python interfaces," *Journal of Open Source Software*, Vol. 6, No. 61, 2021, p. 3145. https://doi.org/10.21105/joss.03145, URL https://joss.theoj.org/papers/10.21105/joss.03145.
- [49] Bezanson, J., Edelman, A., Karpinski, S., and Shah, V. B., "Julia: A Fresh Approach to Numerical Computing," SIAM Review, Vol. 59, No. 1, 2017, pp. 65–98. https://doi.org/10.1137/141000671, URL https://epubs.siam.org/doi/10.1137/141000671.
- [50] Weissinger, J., "The Lift Distribution of Swept-Back Wings," Tech. rep., National Advisory Committee for Aeronautics, 1947.
- [51] Kim, T., Oh, S., and Yee, K., "Improved actuator surface method for wind turbine application," *Renewable Energy*, Vol. 76, 2015, pp. 16–26. https://doi.org/10.1016/j.renene.2014.11.002, URL http://dx.doi.org/10.1016/j.renene.2014.11.002https://linkinghub.elsevier.com/retrieve/pii/S0960148114007162.
- [52] Veldhuis, L. L. M., "Propeller Wing Aerodynamic Interference," Ph.D. thesis, Delft University of Technology, 2005.
- [53] Weber, J., and Brebner, G., "Low-Speed Tests on 45-deg Swept-Back Wings, Part I," Tech. rep., 1951.
- [54] Sinnige, T., de Vries, R., Corte, B. D., Avallone, F., Ragni, D., Eitelberg, G., and Veldhuis, L. L. M., "Unsteady Pylon Loading Caused by Propeller-Slipstream Impingement for Tip-Mounted Propellers," *Journal of Aircraft*, Vol. 55, No. 4, 2018, pp. 1605–1618. https://doi.org/10.2514/1.C034696, URL https://arc.aiaa.org/doi/10.2514/1.C034696.
- [55] Sinnige, T., Stokkermans, T. C., van Arnhem, N., and Veldhuis, L. L., "Aerodynamic performance of a wingtip-mounted tractor propeller configuration in windmilling and energy-harvesting conditions," AIAA Aviation 2019 Forum, No. June, 2019, pp. 1–17. https://doi.org/10.2514/6.2019-3033.

- [56] Sinnige, T., van Arnhem, N., Stokkermans, T. C. A., Eitelberg, G., and Veldhuis, L. L. M., "Wingtip-Mounted Propellers: Aerodynamic Analysis of Interaction Effects and Comparison with Conventional Layout," *Journal of Aircraft*, Vol. 56, No. 1, 2019, pp. 295–312. https://doi.org/10.2514/1.C034978, URL https://arc.aiaa.org/doi/10.2514/1.C034978.
- [57] Chu, S., Linton, D., Verstraete, D., and Thornber, B., "Aerodynamic Analysis of Multi-Propeller/Wing Interaction using the Actuator Surface Model," *AIAA Scitech 2021 Forum*, American Institute of Aeronautics and Astronautics, Reston, Virginia, 2021, pp. 1–15. https://doi.org/10.2514/6.2021-1661, URL https://arc.aiaa.org/doi/10.2514/6.2021-1661.
- [58] van Arnhem, N., "Unconventional Propeller-Airframe Integration for Transport Aircraft Configurations," Ph.D. thesis, Delft University of Technology, 2022.
- [59] van Arnhem, N., Sinnige, T., Stokkermans, T. C., Eitelberg, G., and Veldhuis, L. L., "Aerodynamic Interaction Effects of Tip-Mounted Propellers Installed on the Horizontal Tailplane," 2018 AIAA Aerospace Sciences Meeting, American Institute of Aeronautics and Astronautics, Reston, Virginia, 2018. https://doi.org/10.2514/6.2018-2052, URL https://arc.aiaa.org/doi/10. 2514/6.2018-2052.
- [60] Stokkermans, T. C. A. S., "Aerodynamics of Propellers in Interaction Dominated Flowfields," Ph.D. thesis, TU Delft University, 2020.
- [61] Ahrens, J., Geveci, B., and Law, C., "ParaView: An End-User Tool for Large Data Visualization," Visualization Handbook, Elsevier, 2005.
- [62] Ayachit, U., The ParaView Guide: A Parallel Visualization Application, Kitware, 2015.